Nuclear Instruments and Methods in Physics Research A 332 (1993) 419–443
North-Holland

NUCLEAR
INSTRUMENTS
& METHODS
IN PHYSICS
RESEARCH
Section A

A study of two prototype lead glass electromagnetic calorimeters

B.B. Brabson, R.R. Crittenden, A.R. Dzierba, T. Foxford, J. Gunter, R. Lindenbusch, P.T. Smith, E. Scott, T. Sulanke, S. Teige and Z. Ziliak
Department of Physics, Indiana University, Bloomington, IN 47405, USA

S.U. Chung, C. Olchanski, D.P. Weygand and H.J. Willutzki
Brookhaven National Laboratory, Upton, L.I., NY 11973, USA

A. Soldatov, A. Dushkin, I. Shein, V. Kochetkov and S. Denisov
Institute for High Energy Physics, Protvino, Russian Federation

C.L. Davis
Department of Physics, University of Louisville, Louisville, KY 40292, USA

Z. Bar-Yam, J.P. Dowd and W. Kern
University of Massachusetts Dartmouth, North Dartmouth, MA 02747, USA

L.I. Belzer, V.A. Bodyagin, A.I. Demianov, A.M. Gribushin, V.L. Korotkich, N.A. Kruglov, A.I. Ostrovidov, A.S. Proskuryakov, L.I. Sarycheva and N.B. Sinev
Institute for Nuclear Physics, Moscow State University, Moscow, Russian Federation

T. Adams, J.M. Bishop, R.D. Cady, N.M. Cason, J.M. LoSecco, J.J. Manak, W.D. Shephard, D.L. Stienike, S.A. Taegar and D.R. Thompson
University of Notre Dame, Notre Dame, IN 46556, USA

Received 11 February 1993

Two prototype lead glass calorimeters have been constructed and tested at the AGS at Brookhaven National Lab. The first is a 25-element prototype (P1) which was tested in the A2 beam line using electrons and pions ranging in energy from 0.5 to 5.0 GeV. Results were obtained on energy resolution, the effect on energy resolution of pre-radiators and non-normal incidence, and on e/π separation. The second prototype (P2) has 319 elements and was tested in the A3 beam line using 3.0 and 5.0 GeV electrons and 15.0 GeV negative pions. Results were obtained on position resolution and effective mass resolution. Data were collected requiring multi-photon signatures in the calorimeter. The design, construction, monitoring, readout electronics (including a custom-built fast-encoding ADC system) and testing of the prototypes are described. These calorimeters are prototypes for a 3053-element lead glass calorimeter being built for Brookhaven Experiment 852: a search for mesons with unusual quantum numbers. Quality control procedures are also discussed.

1. Introduction

Lead glass calorimeters have been used for many years, and continue to be used, in high energy physics research in both fixed-target and colliding-beam experiments. A Brookhaven Lab AGS experiment (E852) [1] is currently under construction to search for mesons with unusual quantum numbers and will concentrate on a study of meson states in the 1–3 GeV/c^2 mass range which decay into 0, 1 or 2 charged particles plus photons, through intermediate states such as $\pi^0 \to 2\gamma$, $\eta \to 2\gamma$, and $\omega \to \pi^0\gamma$. The photons will be detected and measured using a 3053-element lead glass calorimeter to be installed in the Multiparticle Spec-

trometer (MPS). An important feature of E852 will be the ability to require such decays as $\pi^0 \to 2\gamma$, $\eta \to 2\gamma$, and $\omega \to \pi^0\gamma$ as part of the event trigger.

In designing the lead glass detector (LGD) for E852, two prototype calorimeters were constructed and tested. A 25-element lead glass prototype calorimeter (P1) was tested using electron beams of energies ranging from 0.5 to 5.0 GeV in the A2 beam line at Brookhaven National Lab (BNL). The energy resolution was determined as well as the effects of pre-radiators and non-normal incidence on energy resolution. The ability to distinguish electrons from pions with P1 was also studied. A second prototype (P2), consisting of 319 modules, was tested using 3.0 and 5.0 GeV electron and 15.0 GeV negative pion beams in the A3 beam line, also at BNL. In the P2 tests the calibration and monitoring procedure was exercised and data were collected on multi-photon final states with and without charged particles. These data will be used in the design of the trigger processor for E852. The all-neutral decays of π^0, η, η', ω, K_S^0, $a_0(980)$, $f_2(1270)$, and $a_2(1320)$ were observed. Results were also obtained on the position resolution and on the effective mass resolution.

The phototube bases used in the P1 and P2 prototypes incorporate a Cockcroft–Walton high voltage system with computer control. E852 will use a custom-built 12-bit ADC system which can digitize in 4 μs. This system and its performance in the P2 tests is described below. A laser-monitoring system was used for both the P1 and P2 tests with two very different light distribution techniques. These are described below. Finally the quality control procedures for the lead glass calorimeter components, the glass blocks and phototubes are also described.

2. Calorimeter components and quality control

2.1. Lead glass

The lead glass was manufactured in Russia [2] and is the type F8-00. The chemical composition of this glass is 45% PbO, 42.8% SiO_2, 10.4% K_2O and 1.8% Na_2O and has a density of 3.6 gm/cm^3, a radiation length of 3.1 cm, a nuclear collision length of 22.5 cm and an index of refraction of 1.62. The dimensions of each block are $4 \times 4 \times 45$ cm^3. The transverse dimensions of an individual block are set by a number of considerations including the transverse size of the electromagnetic showers (≈ 3 cm). The transverse dimensions should be small enough so that a typical shower will spread into neighboring modules permitting good shower localization. Making the transverse dimensions much smaller than the shower size is impractical since the number of Cherenkov photons produced in a given block decreases and losses by reflection at the block walls can become important. Other considerations include matching the transverse dimension to phototube diameter and keeping the number of channels (glass blocks, phototubes, bases, cables, ADCs) down to a reasonable number. A study by others [3] concluded that 3.8 to 4.0 cm is the optimal transverse dimension of lead glass blocks for shower energies expected in E852. The longitudinal dimension of the blocks should be long enough to fully contain the most energetic showers (20 GeV for E852) however increasing the length much beyond full containment will cause degradation in energy resolution due to the absorption of Cherenkov light. For F8 glass the length for 98% containment is about 41 cm.

In E852 the target-to-calorimeter distance was set at 5 m to guarantee that the photons from the most energetic π^0's be separated by at least 8 cm at the front face of LGD. The dimensions and aspect ratio of the LGD are designed to match the MPS magnet aperture. The placement of the target within the magnet is chosen to allow for sufficient tracking length within the magnetic field to insure good momentum resolution for charged particles while at the same time having the target close enough to the aperture to allow photons to escape through the magnet and be detected by the LGD. All these considerations lead to an LGD with 3053 elements in 71 columns and 43 rows or an active area 172 cm high by 284 cm wide. With this number of channels, quality control is important in the LGD construction.

2.1.1. Transmission measurements

The optical transmission of a sample of 44 blocks was measured using a Shimazu spectrophotometer [4]. The transmission measurement was made along the 4 cm thickness. The results are shown in fig. 1. No attempt was made to correct for the effect of reflection from the glass surfaces.

2.1.2. Measurement of lead glass block dimensions

Since the full scale LGD will be stacked in a 43×71 element array, stringent tolerances are required for the transverse dimensions of the glass blocks to minimize mechanical stresses and voids between blocks. The transverse dimensions of the blocks were specified to be 4.0 cm by 4.0 cm with a tolerance of 50 μm. Surface flatness was specified by requiring that two imaginary parallel planes separated by no more than 70 μm would contain all points on a surface of the block.

In order to measure how well the tolerances were met, a computer-controlled (through CAMAC) lead glass block measuring device was constructed. A schematic is shown in fig. 2. A measuring stage moves up and down along the full length of the block under computer control and stops at a number of points

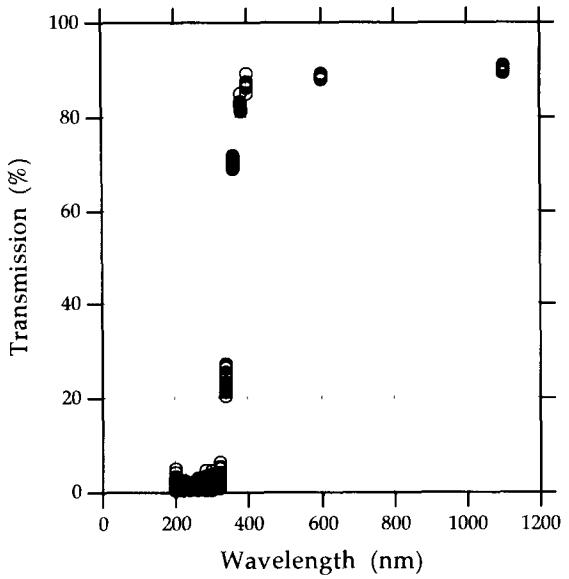

Fig. 1. Measurement of the transmission of 44 blocks along the 4 cm transverse dimension. The measurements were made with a Shimazu spectrophotometer [4]. No attempt was made to correct for reflections from the glass surfaces.

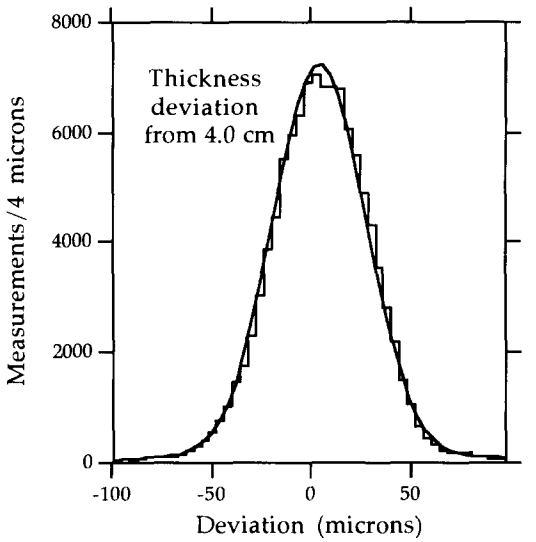

Fig. 3. The distribution of thickness measurements (expressed in deviations from 4.0 cm) for a sample of 3200 lead glass blocks. The Gaussian fit yields a mean of 6.8 μm and a σ of 24.0 μm.

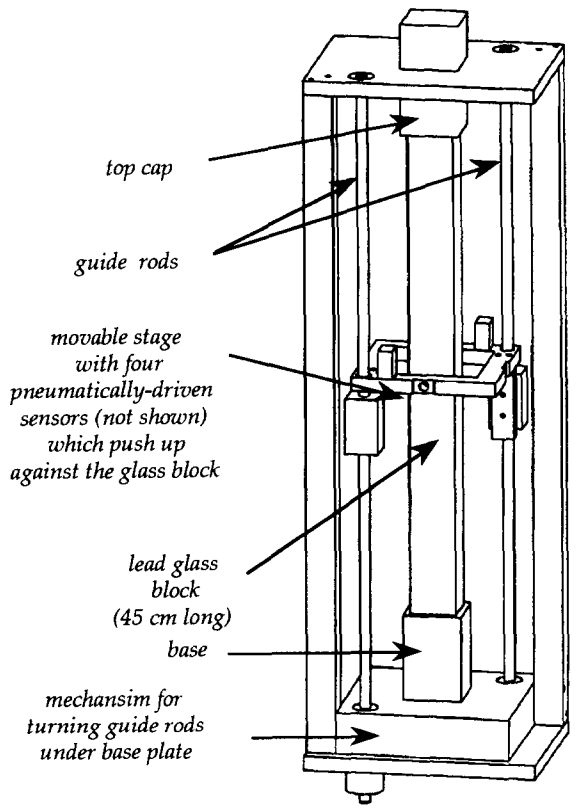

Fig. 2. A schematic of the block measuring apparatus to check the tolerance of the transverse dimensions of the lead glass blocks and to also measure taper.

(typically 17) along the block to make a measurement. The stage is linked to guide rods [5] which convert the rotation of the rods into vertical motion of the stage. The guide rods are turned by a stepping motor. Riding on the measuring stage are four pneumatic probes [6], operated at 20 psi, which measure the distance between the edge of the block and the probe zero point. The block measurer was calibrated and the temperature effects studied. At constant temperature ($\pm$10°C) the thickness measurements are reproducible to $\pm$1.5 μm.

A block to be measured has a bar-code label attached to one end of the block. The label is read by a wand and the bar identifier and subsequent measurements are logged by computer. The measuring pass starts by measuring the aluminum base which holds the block, followed by a measurement of the cap which holds the top end of the block. Following this the stage moves down the block. At each point of measurement the stage stops, the probes push up against the blocks and then are retracted. A typical measurement, including reading the bar code and inserting the block, takes about 5 min. The deviations from 4.0 cm for 3200 blocks is shown in fig. 3. A Gaussian fit yields an average deviation of 6.8 μm and a σ of 33.7 μm. If a $\pm$75 μm cut is imposed on the thickness tolerance, 95% of the blocks are accepted. A measurement of the taper of the blocks was also made. The distribution of taper measurements, expressed in units of microns per cm of block length, yields a Gaussian distribution with a average of 0.02 μm/cm and a σ of 0.3 μm/cm.

2.2. Phototubes

The phototubes used in the prototype detectors and the LGD are FEU-84-3, manufactured in Russia. They are 12 stage phototubes with a 3.0 cm diameter SbNa–KCs (antimony–sodium–potassium–cesium) photocathode.

2.2.1. Mechanical tests

The outside phototube diameter is specified by the manufacturer as no more than 3.4 cm and the length (not including pins) is typically 10.0 cm. A simple yes/no test checked for phototubes which had the incorrect length or non-centered pins. An aluminum tube was machined with an inner diameter of 3.49 cm. The phototube was inserted into a socket and the socket and phototube inserted in the aluminum tube. Insertion is not possible if the pins were off-center. The top of the phototube was required to be at least flush with, or up to 0.4 cm over, the top of the aluminum tube. Of the phototubes tested, 83.6% passed, 14.2% were too short, 0.4% were too long and 1.8% had off-center pins.

2.2.2. Quantum efficiency

The measurement of the absolute quantum efficiency of an initial sample of 30 phototubes supplied by the manufacturer proceeded in two steps. First, the number of photoelectrons emitted by a phototube when illuminated by a stable (but uncalibrated) light source was determined. This produced a ranking or relative measurement of quantum efficiencies of the phototubes in the sample. Second, the normalization of these relative efficiencies was determined by obtaining an absolute measurement of the quantum efficiency of three phototubes by Hamamatsu Inc. using a calibrated source. The resulting quantum efficiency, as a function of wavelength, for the three phototubes is shown in fig. 4.

To determine the relative quantum efficiency of the tubes in the sample, the relative number of photoelectrons emitted when the tube was exposed to a stable light source was measured. The light source was a piece of type NE110 scintillator, 0.5 in. × 0.5 in. and 3.0 in. thick, attached to a 1.5 μCi ^{241}Am source. The phototube under test was placed 2 in. from the scintillator. The efficiency was determined by measuring the rate of pulses over a 0.7 mV threshold normalized to the rate of pulses over a 100 mV threshold in a trigger phototube. The trigger phototube was an RCA 8575 attached directly to the scintillator. The test setup used initially in these quality control measurements is shown schematically in fig. 5.

With a photocathode to scintillator distance of 2 in., the geometric acceptance for photons is low enough so

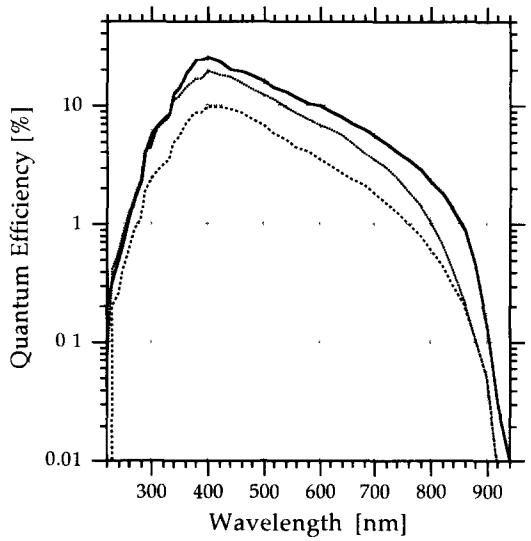

Fig. 4. The absolute quantum efficiency of three FEU-84-3 phototubes as measured by Hamamatsu Inc. using a calibrated source. Three tubes were selected, using the method described in the text, as having relatively high, medium and low relative quantum efficiencies.

that the mean number of photoelectrons, $\langle n \rangle$ is related to the efficiency, ε, by Poisson statistics:

$$\varepsilon = 1 - e^{-\langle n \rangle}. \quad (1)$$

The mean number of photoelectrons used here is actually the relative number of photoelectrons which depends on the quantum efficiency of the phototube, the intensity of the light source and geometric factors affecting the light collection efficiency. Since ^{241}Am is an α emitter and the α's stop in the scintillator, the light source can be expected to be extremely stable from pulse to pulse. The geometric factors were held constant from phototube to phototube by fixing both the photocathode to scintillator distance and the orientation of the photocathode. Thus $\langle n \rangle$ is proportional to the quantum efficiency.

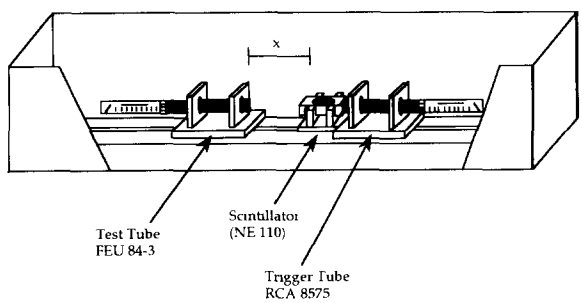

Fig. 5. The phototube quality control measuring device used in initial measurements. This was later replaced by a device which could make quality control measurements on four phototubes simultaneously.

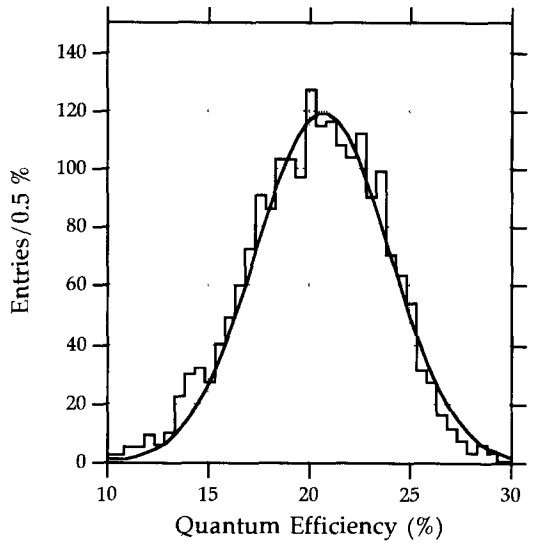

Fig. 6. The distribution in absolute quantum efficiency, at 1900 V, for a sample of 1000 phototubes. A fit to a Gaussian distribution yields a mean of 21% and a σ of 3%.

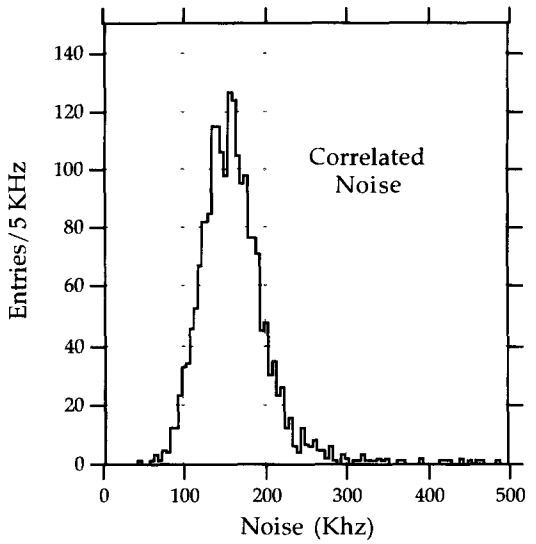

Fig 7. Distribution in correlated noise rate sampled 600 ns after the trigger pulse, at 1900 V, for 1000 phototubes.

For measuring the relative quantum efficiencies of the final sample of phototubes, a four-stage test station was constructed, based on the design of the initial test station. The phototube under test is labeled with a bar code, read by the computer and placed in one of the four stations each of which is also identified with a bar code and read out. When all four test phototubes are in place, the light-tight box is closed and the quantum efficiency and noise rates measured. The noise rate measurements are described below. The distribution in absolute quantum efficiency, obtained from these results and normalizing using the reference phototubes discussed above, at an operating high voltage of 1900 V, is shown in fig. 6. The distribution is Gaussian with a mean of 21% and a σ equal to 3%.

2.2.3. Noise rates

Two noise rates were measured, the random noise rate and the noise associated with a real signal pulse (*after-pulsing* or *correlated noise*). The random noise rate was defined to be the rate of pulses over 0.7 mV in the phototube under test not in coincidence with a pulse over 100 mV in the trigger phototube. Correlated noise was defined as the probability of a pulse over 0.7 mV in the test phototube occurring within some variable time after a trigger pulse in the trigger phototube. The same apparatus was used for these measurements as for the measurements of the quantum efficiency.

The correlated noise was measured for the entire sample at a time 600 ns after a trigger pulse. Fig. 7 shows the distribution of correlated noise rate. The correlated noise was also measured as a function of the delay time for a typical phototube. The result of this measurement (see fig. 8) shows that there is an exponential decay of this noise rate in time with a decay constant of ≈ 500 ns. Fig. 9 shows the distribution of the random noise rate measurements for this sample of phototubes. The noise rates were measured at an operating high voltage of 1900 V.

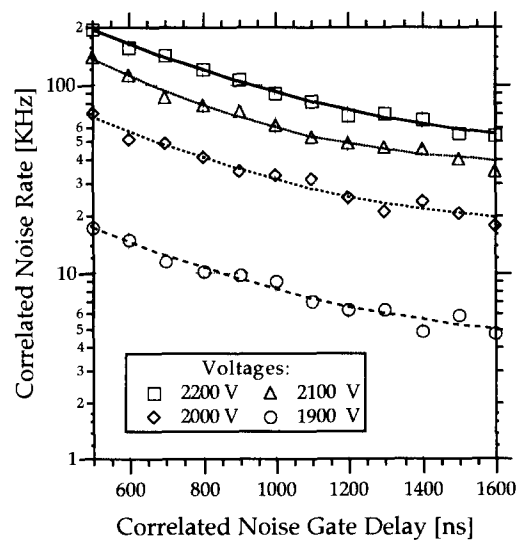

Fig 8. The correlated noise rate, measured in a 600 ns window, as a function of gate delay, for a representative phototube.

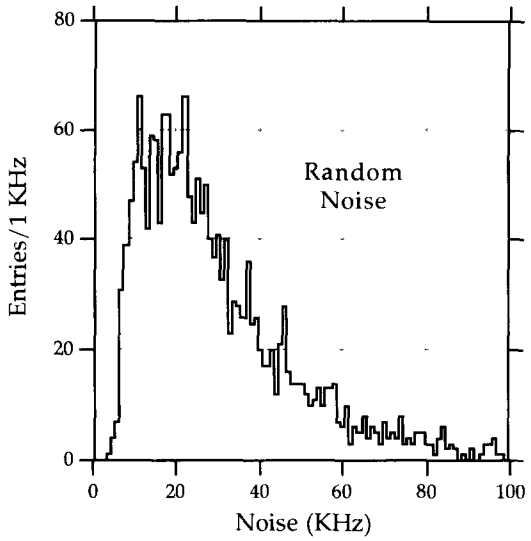

Fig. 9. Distribution in random noise, at 1900 V, for 1000 phototubes.

2.3. High voltage system

A computer-controlled, Cockcroft–Walton high voltage power supply is installed in each phototube base. This system, an overview of which is shown in fig. 10, consists of a power supply and the CAMAC high voltage controller, (which can drive 4096 phototube bases), a main station and individual phototube bases. The power supplies and controller reside in the experiment control room and the main station at the lead glass detector. The bases are daisy-chained to a ribbon cable which transmits DC power and address and data signals. In the drawing of fig. 10 the distribution system for the full LGD (71 columns and 43 rows) is shown as 71 branches with each branch feeding 43 bases. In the P2 tests, described later in this paper, 18 branches with 18 bases per branch were used.

The high voltage is set by issuing CAMAC commands from a computer. Each command includes a 12-bit base address (the lower 8 bits specify the bases in a group of 256 bases and the higher 4 bits specify

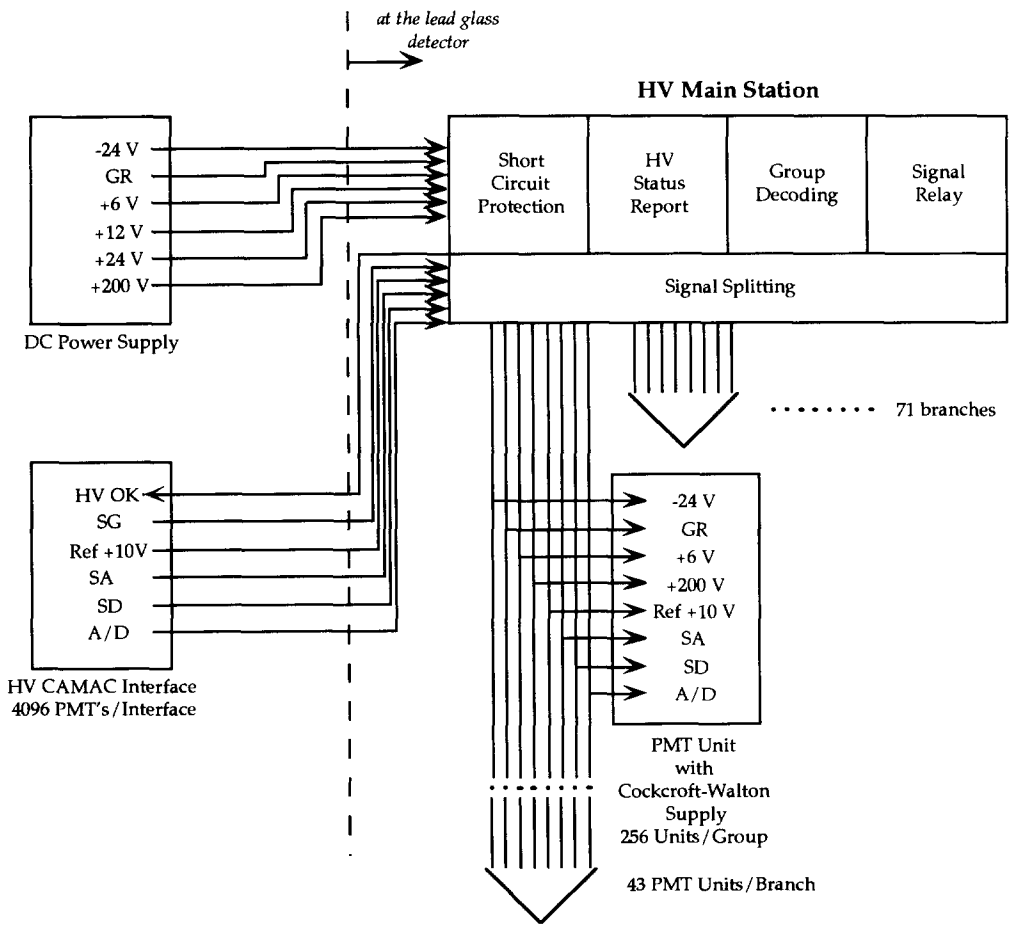

Fig. 10. Overview of the Cockcroft–Walton high voltage distribution system. Please see the text for details and definition of signal names.

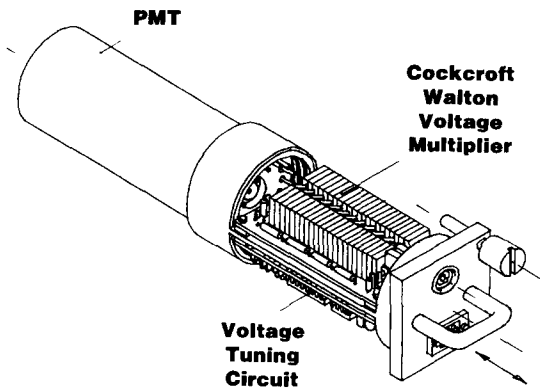

Fig. 11. A drawing of a high voltage base assembly attached to a phototube.

the group). This is followed by a 10-bit high voltage code. These data are sent over three signal lines: address synchronization (SA), data synchronization (SD) and the data (D). The commands are transmitted at 100 kbits/s so setting the high voltage on a single phototube takes 0.22 ms.

A phototube base drawing is shown in fig. 11. The base is 14 cm long (about 8 cm occupied by electronics) and 3.9 cm × 3.9 cm in the transverse dimension. The base includes a spring-driven socket (the spring stroke is 1.0 cm) to push the phototube against the lead glass and a rear connector panel.

The base functions are shown in fig. 12. The ADDRESS REGISTER is an 8-bit shift register which uses the address synchronization pulses transmitted on the SA line to record the base address sent over the data bus (D). The ADDRESS IDENTIFICATION is a code comparator and identifies the individual address of the base. Only for the addressed base are the data synchronization pulses on the SD line allowed to pass to the DATA REGISTER, which stores the high voltage code. This code is sent to a 10-bit DAC. The feedback resistor of the DAC is under negative voltage, which is proportional to the output high voltage and which is supplied from a BUFFER AMPLIFIER, fed through a divider with the voltage from the lowest stage of the VOLTAGE MULTIPLIER. The positive reference voltage, applied to the DAC, results in an output DAC current proportional to the difference between the required and actual voltage values. This difference, or error, signal is fed into a ERROR AMPLIFIER whose output is connected to a MODULATOR converting the d.c. into a 50 kHz a.c. signal. This signal is then amplified by an amplifier whose gain is ≈ 20, and whose output impedance is less than 1 kΩ. Finally the output is applied to a multi-stage diode/capacitor VOLTAGE MULTIPLIER, the outputs of which are directly connected to the corresponding outputs of the phototube. The VOLTAGE MULTIPLIER is shunted by a 1 GΩ resistor in order to create a permanent discharge current from the VOLTAGE MULTIPLIER capacitors with a time constant of order 1 s. This makes it possible to continually adjust the output high voltage independent of whether a current is present in the phototube.

All the logic elements (registers and comparators) and the DAC exist on a single, custom-built chip manufactured in Russia.

This system allows for the control of 4096 phototubes with a maximum voltage of 2048 V in 2 V steps. The output voltage is stable to within ±0.2% for temperature variations of 10°C and average phototube currents of 0 to 0.1 mA. The power consumption per

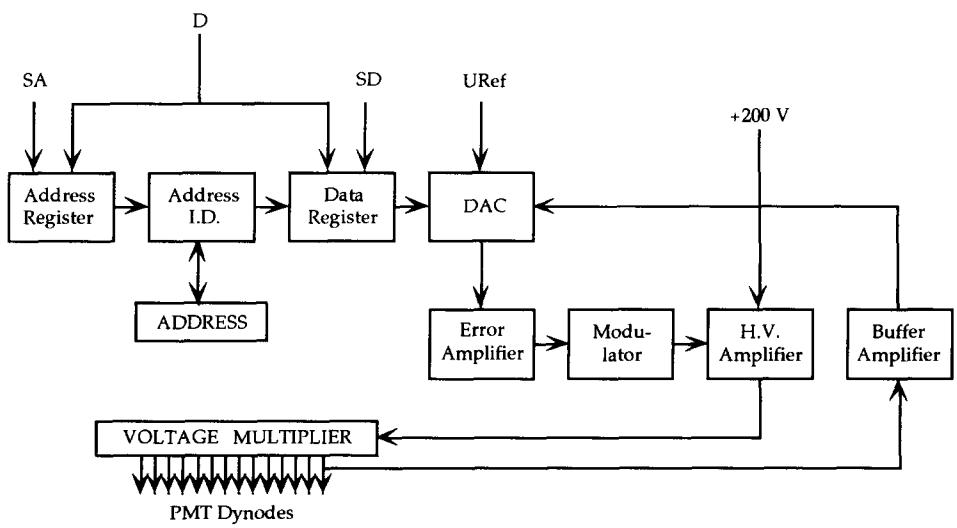

Fig. 12. Block diagram showing the function of the phototube base. Please see the text for definitions of signal names.

base is 0.3 W. This system was used in both prototype calorimeter tests described below.

3. 25-element prototype (P1)

3.1. Mechanical construction

The 25-element prototype consisted of a 5 by 5 array of lead glass blocks held in an aluminum framework. The blocks and the framework holding them were contained in a $18 \times 18 \times 36$ in^3 light-tight, temperature-controlled box. The box was made from 1/32-in. thick aluminum sheet on a 3/4-in. skeleton. The front face was equivalent to 1% of a radiation length of material. The box was insulated with 3/4-in. thick Styrofoam on its interior. The temperature in the interior was controlled by a solid state refrigerator/heater [7] to within ± 1°F.

For the beam tests, the detector and the temperature controlled box were mounted on a table that allowed the system to be translated in both directions perpendicular to the beam axis. Two axes of rotation (both perpendicular to the beam) were provided by a smaller table mounted on the larger translating table. These rotational degrees of freedom allowed determination of the response of the detector to non-normally incident particles.

The blocks were wrapped in 0.0005-in. thick aluminized mylar for optical isolation. Each phototube was contained in an aluminum canister along with its base. The canisters were attached to aluminum plates glued to the back faces of the blocks. Optical fibers for monitoring were attached to connectors on these plates. Signal and high voltage connections were made with feed-throughs on the back plane of the temperature controlled box.

3.2. Optical coupling

The full scale LGD will operate in the fringe field of the MPS analyzing magnet in a region where the field can be as large as 100 G. As part of the P1 studies, an optical coupling was tested which would allow one to extend the 0.5-mm thick μ-metal shielding 0.7 in. beyond the photocathode, a distance corresponding to about 1/2 of the photocathode diameter. To achieve this, the photocathode was optically coupled to the block by a 0.7-in. thick cylindrical light guide made of optical gel [8].

A series of tests using cosmic ray muons were performed to determine the characteristics of the detector in an approximate way and to determine if the design was adequate to give sensitivity to a single, minimum ionizing particle. The detector as assembled prior to the beam tests did not have the aluminized mylar wrapping on the light guides. The energy resolution of the detector to cosmic ray muons was a factor of four worse than anticipated from Monte Carlo predictions. It was determined that a large fraction of the Cherenkov light produced by these muons was lost through the sides of the light guide because of the index of refraction mismatch with the lead glass. As a result, the outer, cylindrical surface of the light guide was wrapped in 0.005-in. thick aluminized Mylar.

3.3. Monitoring

Phototube gain was monitored by a nitrogen laser/photodiode system. The output pulse of the laser was directed into an optical fiber attached to the laser. The other end of the fiber illuminated a photodiode and the end of a bundle of 32 secondary fibers that carried output pulses to the individual modules. Gain was monitored by the response of the individual modules normalized to the photodiode response analyzed as a function of time

The nitrogen laser used [9] has an average power of 6 mW, and a maximum pulse energy 400 μJ, with peak emission at 337 nm. Neither the fibers nor the glass transmit light at the primary emission peak of this laser but it was found to produce sufficient light with a fast enough rise time to be suitable for the purpose of monitoring gain.

Since pulse-to-pulse variations in the total laser power were as large as 10%, the output intensity of the laser was measured for each pulse. A single fiber from the laser illuminated a photodiode [10] at an angle of incidence of 45°. A portion of the light was reflected and directed into the fiber bundle described below. This diode was chosen because of its very fast rise time (≈ 1 ns) and its temperature stability (0.1% per °C). The output of the photodiode was converted to digital information by the same ADCs used to read out the detector.

The light from the laser was transmitted to the individual modules of the detector by a bundle of 32 optical fibers [11]. Variations in the fiber size (and perhaps transmission) from fiber to fiber yielded variations of a factor of two in total light output delivered to each module. These variations were not sufficiently large to exceed the dynamic range of the ADCs so they were deemed acceptable.

Since the P1 beam tests spanned a short period of time, the monitoring system was used primarily to verify that the modules were turned on. However, the P1 detector was used after the beam tests to look at the response to cosmic ray muons over a period of four months. From these measurements it was determined that the system was stable to within 1%.

3.4. Readout and data acquisition

The analog to digital converters used in this device were LeCroy Research Systems type 4300 fast encoding and readout (FERA) ADCs. These are CAMAC devices packaged 16 to a single wide slot with a conversion time for 11 bit resolution of 8.5 μs. The data acquisition computer was a VAX station II/GPX.

The zero point offset (pedestal) of the ADCs was determined by averaging the readout value for each channel after gating the ADC with no input signal. The distributions of pedestal events were narrow (σ less than 1 count) for all channels used in this analysis. Pedestals were accumulated at the end of each day of running during the electron beam tests.

3.5. Electron beam, pre-beam calibration and initial calibration

The energy response of P1 prototype was measured in a momentum analyzed, tagged electron beam at BNL. The A2 test beam provides positive or negative secondary particles produced at 17° to a primary proton beam of 28 GeV. A quadrupole doublet provides focusing and a dipole and adjustable collimator control flux and momentum. Energies between 0.5 and 9.6

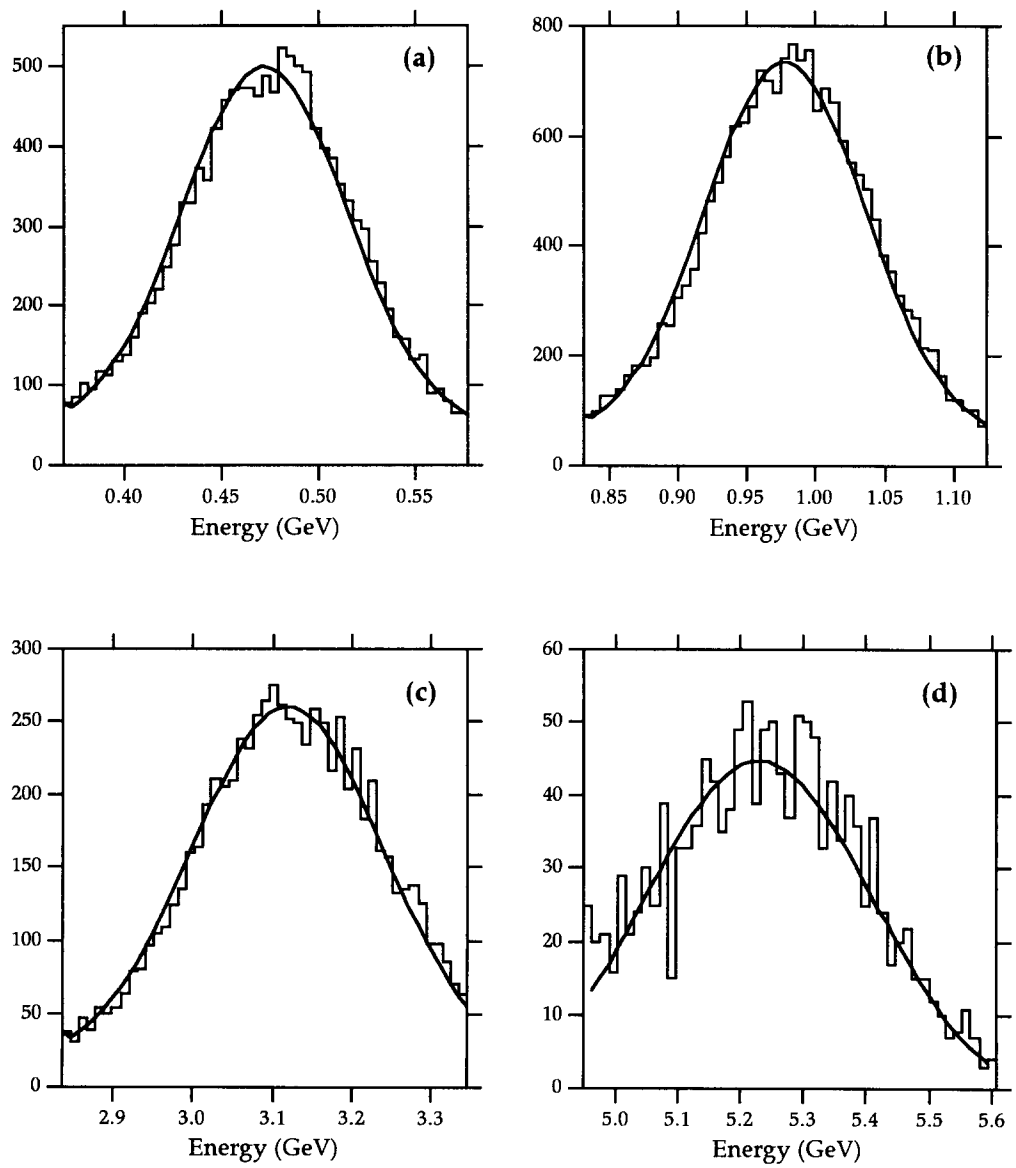

Fig. 13. Observed energy deposition at (a) 0.5 GeV, (b) 1.0 GeV, (c) 3.0 GeV, and (d) 5.0 GeV.

GeV are available. Electrons are tagged by a pressurized threshold Cherenkov counter. Typical electron content is 3% at 0.5 GeV and 0.5% at 3 GeV. The momentum bite, $\Delta p/p$, is adjustable by tuning the collimator. The data presented here were taken with the collimator adjusted to provide $\Delta p/p < 1\%$. Momentum was selected by adjusting the current to the dipole.

The relative gain versus voltage characteristics for the modules were obtained by illuminating an assembled detector module with light from a pulsed LED [12] and analyzing the pulse height distribution as a function of high voltage. The absolute value of the gain could not be determined by this method because the intensity of the input light pulse was unknown, as was the efficiency of the coupling of the tube to the lead glass module. Even with these limitations, the measurements were the basis for setting the initial values of the high voltage.

When the detector was in place in the A2 beam line the operating voltages of the phototubes were determined by illuminating the center of each block with a 3 GeV electron beam. The pulse height distributions were analyzed with peak finding techniques and the voltages adjusted so that each module had its peak in approximately the same ADC channel.

3.6. Energy resolution

Data were taken with incident electrons with energies of 0.5, 1.0, 1.5, 3.0 and 5.0 GeV at normal and non-normal angles of incidence with a minimal amount of material in front of the detector. In addition, data at 1.0 and 3.0 GeV were taken with 0.7 and 1.7 radiation lengths of material in front of the device.

3.6.1. Calibration algorithm

To convert the pulse height determined by the ADC to energy deposited in a module, a set of calibration constants was determined. To find these constants the detector was illuminated by a monoenergetic, tagged electron beam and a χ^2 minimization method applied. The χ^2 of the energy measurement is given by:

$$\chi^2 = \sum_{j=1}^{N} \frac{\left(E_b - \sum_{i}^{25} c_i P_{ij}\right)^2}{\sigma^2}, \tag{2}$$

where E_b is the energy of the incident beam, c_i is the calibration constant of the ith module, P_{ij} is the pulse height in the ith module for the jth event and σ is the resolution, independent of module. The sample contains N events.

Assuming that the resolution is independent of module, the c_i can be varied to minimize the χ^2 by solving the following equation, obtained from differentiating the above with respect to the c_i:

$$\sum_{j=1}^{N} \left(E_b - \sum_{i=1}^{25} c_i P_{ij}\right) P_{lj} = 0. \tag{3}$$

This can be put in an explicitly linear form by writing:

$$P'_{li} = \sum_{j=1}^{N} P_{lj} P_{ij}$$

$$V_l = E_b \sum_{j=1}^{N} P_{lj}$$

which yields:

$$V = \mathbf{P}'c, \tag{4}$$

An initial set of calibration constants, determined by the data from the single block illumination, was chosen. The above equation was solved to determine a new set of calibration constants. The procedure was iterated until the maximum change in any calibration constant was less than 0.5%.

3.6.2. Resolution function

The observed deposited energy distributions for nominal beam energies of 0.5, 1.0, 3.0 and 5.0 GeV are shown in figs. 13a through 13d respectively along with fitted Gaussian curves. The results of the fits are shown in table 1. The resolution is fitted to a function of the form:

$$\frac{\sigma}{E} = \left(a + \frac{b}{\sqrt{E}}\right)\%, \tag{5}$$

where the nominal beam energy, in GeV, was used. The results yield 1.18% for a, the so-called floor term, and 5.12 $\mathrm{GeV}^{1/2}$ for b, the term which takes into account photoelectron statistics. The fit result is shown in fig. 14. The fitted relationship between the nominal beam energy, E_b, and the measured energy, E_m, is given by:

$$E_b \propto E_m^{0.97} \tag{6}$$

and shows the non-linearity of the detector.

Table 1
Fits of the observed energy deposition to a Gaussian distribution

Nominal beam energy [GeV]	Energy [GeV]	σ [GeV]
0.5	0.47 ± 0.001	0.043 ± 0.001
1.0	0.99 ± 0.001	0.060 ± 0.001
3.0	3.12 ± 0.002	0.121 ± 0.005
5.0	5.23 ± 0.006	0.184 ± 0.018

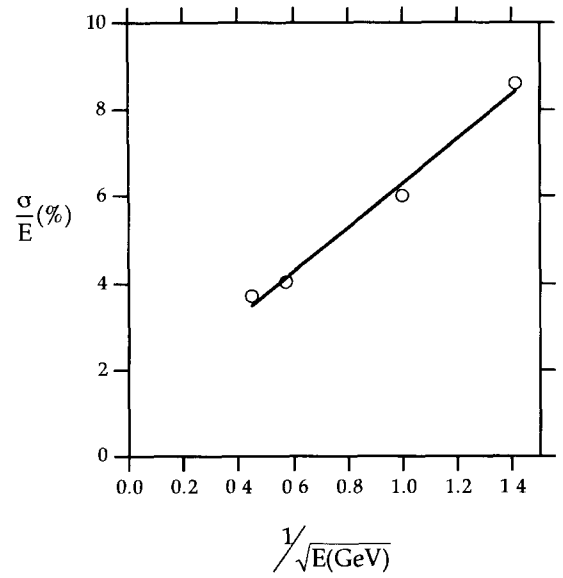

Fig. 14. A fit of the energy resolutions listed in table 1 to a function of the form of eq. (5).

3.6.3. Effect of pre-radiator on energy resolution

The effect on energy resolution of pre-radiator placed against the front face of the detector was investigated at incident electron energies of 1.0 and 3.0 GeV. In one case steel amounting to 0.7 radiation length was used and in the other case steel and lead with a total thickness corresponding to 1.7 radiation lengths was used. The results are summarized in table 2 where we show the decrease in the mean observed energy, ΔE, and the factor by which the observed resolution increases.

3.6.4. Effect of angle of incidence on energy resolution

The response to non-normally incident electrons was investigated by rotating the detector relative to the beam. Data were taken at 0.5, 1.0 and 3.0 GeV with tagged electrons at 4 angles. The rear of the detector was elevated to give simple angles of 5° and 10° to the incident beam. A further rotation of 15° about a vertical axis gave data at a compound angle of 18°. Data were taken at the above energies at normal incidence for comparison. In the following, these data sets are referred to as 0°, 5°, 10° and 18°.

The detector was calibrated independently for each angle. This approach is justified by noting that factors such as optical coupling of the phototube to the lead glass depend on the angle of incidence of the Cherenkov photons on the interface. Fig. 15 shows the width (σ) of the energy response as a function of angle for the three energies investigated. There is no significant evidence for a systematic change in resolution as a function of angle of incidence in these data. Fig. 16 shows the average of the energy measurement distribution as a function of angle. Again, no systematic effects are observed.

3.7. e/π separation

Others have studied the response of lead glass calorimeters to electrons compared to hadrons [13]. The requirement that the incident beam particle be tagged as an electron was removed to investigate the response to hadrons. Fig. 17 shows the distribution of energy deposition due to 3.0, 5.0, 7.0 and 9.6 GeV hadrons. At 3 GeV the beam was known to contain approximately 0.5% electrons, the remainder was as-

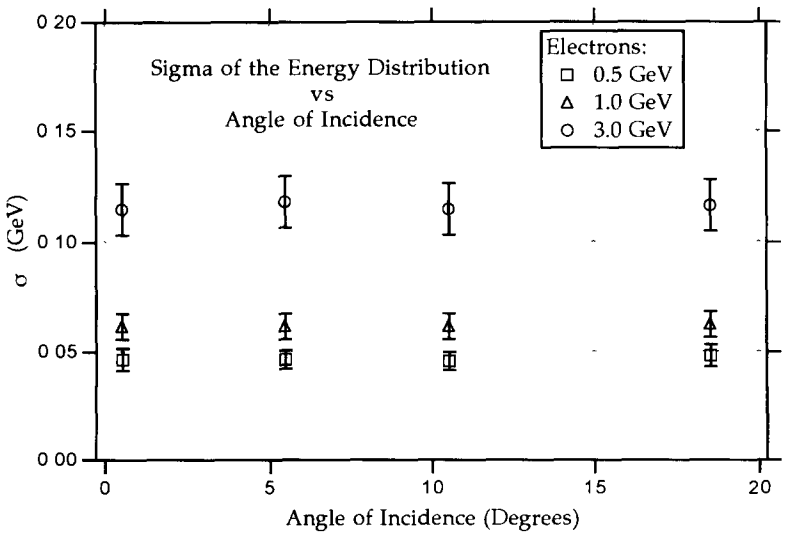

Fig. 15. Dependence of the width (σ) of the observed energy distribution as a function of angle of incidence.

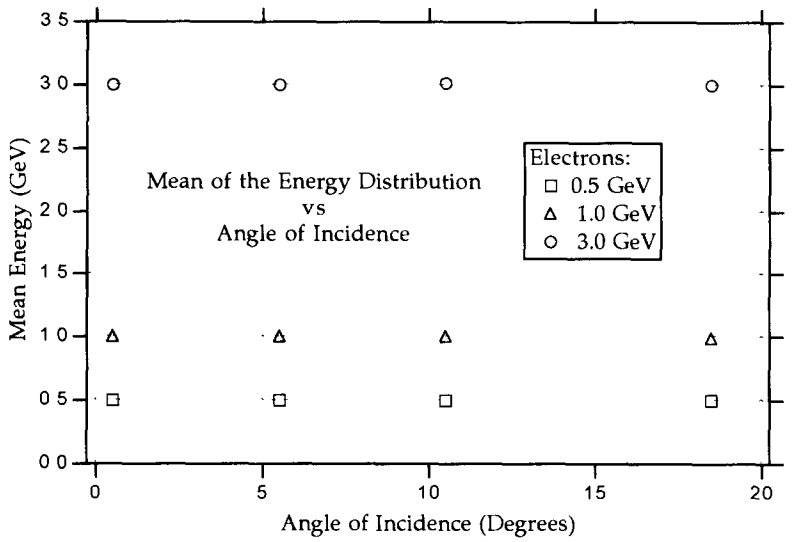

Fig. 16. Dependence of the mean of the observed energy distribution as a function of angle of incidence.

sumed to be pions. The peak associated with electrons is visible in the 3 GeV data and is also shown in the insert distribution of fig. 17. The distributions can be characterized as consisting of two components, the energy deposition of a single minimum ionizing particle plus a decreasing exponential. A fit to the 3 GeV data shows that the probability that a pion deposit energy consistent with that of an electron $\pm 3\sigma$ was 0.01.

The measurements of the energy response to hadrons only shows that there is a non-zero probability that the observed energy deposition of a pion is consistent with that of an electron. However, shower shape information can also be used to reduce the probability of electron misidentification. An energy weighted average radius for the shower is defined as:

$$R = \frac{\sum_{i=1}^{25} E_i \sqrt{(x_i - \langle x \rangle)^2 + (y_i - \langle y \rangle)^2}}{\sum_{i=1}^{25} E_i}, \qquad (7)$$

where E_i is the energy deposited in the ith block and (x_i, y_i) are the coordinates of the ith block. The average coordinate, for example $\langle x \rangle$, is defined as:

$$\langle x \rangle = \frac{\sum_{i=1}^{25} E_i x_i}{\sum_{i=1}^{25} E_i}. \qquad (8)$$

Table 2
Effect of pre-radiator on energy resolution

Beam energy [GeV]	Preradiator thickness [Rad Len]	ΔE [MeV]	$\frac{\sigma(\text{with pre-radiator})}{\sigma(\text{without pre-radiator})}$
1.0	0.7	30	1.0
1.0	1.7	100	1.2
3.0	0.7	40	1.0
3.0	1.7	180	1.1

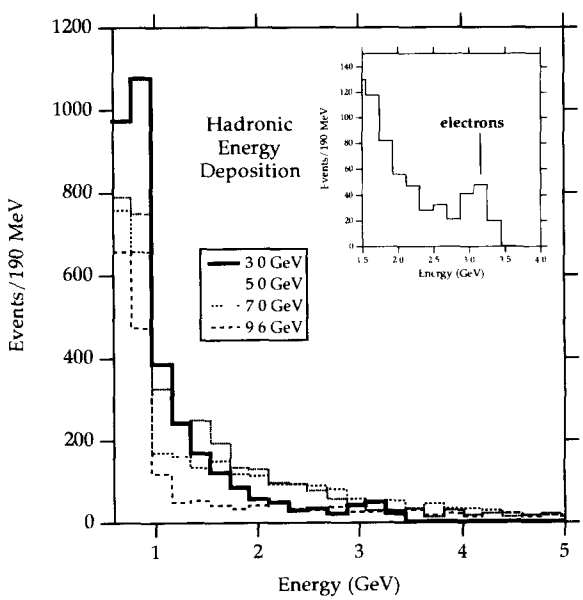

Fig. 17. The energy deposition observed for untagged 3.0, 5.0, 7.0 and 9.6 GeV beam particles, assumed to be primarily hadrons. The insert shows the portion of the 3.0 GeV spectrum showing an electron peak.

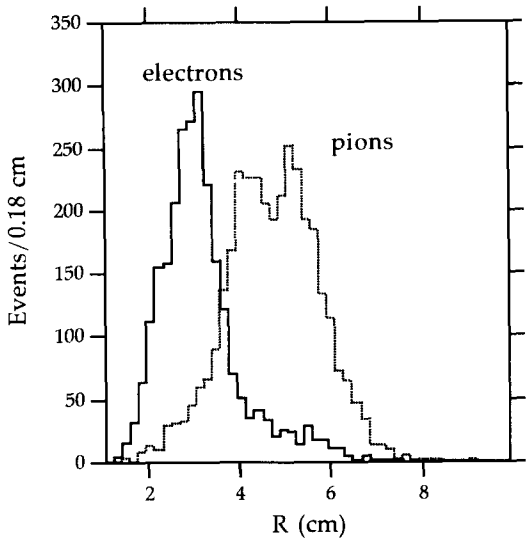

Fig. 18. The distribution in the parameter describing the transverse shower size (see eq. (7)). The distribution is shown separately for 3 GeV beam particles tagged as electrons and untagged particles, assumed to be pions.

Fig. 18 shows the distribution in R as measured with tagged 3 GeV electrons and with an untagged 3 GeV negative beam. By choosing R less than 4 cm, 75% of the pions are rejected while 90% of the electrons survive giving an additional factor of four in π/e rejection for an overall rejection factor of 400. If the electron acceptance is allowed to fall to 50%, by choosing R to be less than 2.9 cm, and the energy deposition requirement replaced by $\pm 2\sigma$ a π/e rejection factor of 1500 can be obtained. The data are inadequate for a meaningful investigation of correlations between energy deposition and shower shape parameters.

4. 324-element prototype (P2)

The P2 prototype was built and tested with a number of goals in mind. These included the development of an efficient calibration procedure and the collection of data on multi-photon final states to be used in designing algorithms for the final trigger processor. The P2 detector is shown schematically in fig. 19.

4.1. Mechanical construction

The prototype consists of 324 blocks arranged in a stack of 18 columns with 18 blocks per column. A block near the middle was removed and replaced with an aluminum channel to allow passage for the beam. As in P1, the blocks were wrapped in 0.0005-in. thick aluminized Mylar for optical isolation. The stack was held firmly in an aluminum frame by plates which pushed

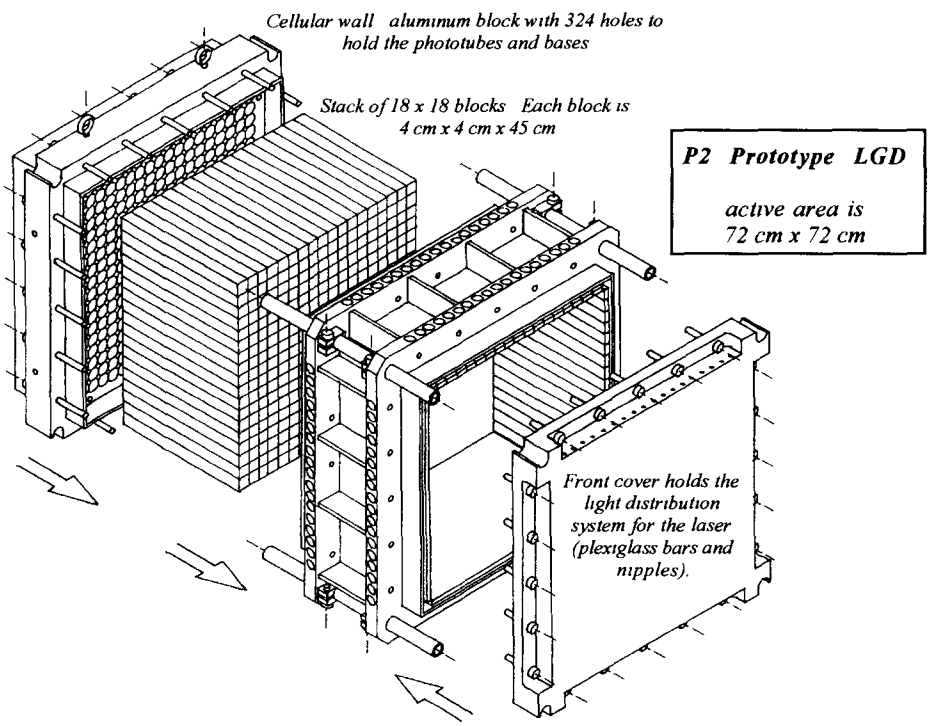

Fig. 19. Schematic drawing of the P2 prototype.

against the stack downwards and from the sides. The pushing action was by means of screws in the sides of the frame. The phototubes and bases were held in registration to the glass stack by means of a cellular wall, an 8-in. thick aluminum plate with 324 holes. The back of the cellular wall had tapped holes. The base/phototube assemblies were inserted and the back plate of the base screwed into the back of the cellular wall. The phototubes simply pushed up against the lead glass. There was no other optical coupling. Finally, the 3/8-in. thick aluminum front cover of P2 supported an array of 18 Plexiglas bars with nipples used as the laser light distribution system. This is described in more detail below.

4.2. Transporter

The assembly shown in fig. 19 was placed atop a transporter [14]. This transporter had sufficient range of travel horizontally and vertically to position each block of the array in the calibration beam. This transporter was outfitted with the motor drive system and associated control system [15] and interlocks [16] now in use in the transporter for the full LGD. As part of the calibration of the detector, each block must be positioned in an electron calibration beam with a precision better than 1 mm. The calibration procedure used for the P2 test, and planned for the full LGD, involves starting the transporter, positioning a module in the beam, and stopping to collect data in one or two accelerator spills. The process then repeats for the next block. The vertical speed is 6 in./min and the horizontal speed is 12 in./min. The acceleration/deceleration ramp is 1 s in both directions. The motion is controlled by computer. The vertical and horizontal positions are read out using shaft encoders [17] coupled to the drive mechanism. The software drives the transporter to a given location by specifying the number of steps the stepping motor should move and then verifies independently that it arrived at the expected location by reading the position encoders.

4.3. Electronics

4.3.1. ADCs

A unique feature of E852 is the ability to find energy clusters, reconstruct photon momenta and calculate effective masses as part of the trigger requirement. In order to accomplish this, fast and high resolution ADCs are needed to digitize the signals from the LGD phototubes. High resolution is needed first, to find the photon clusters in an environment including other photon showers and hadron showers, second, to locate photon positions based on the energy distribution in a cluster of modules and third, reconstruct effective masses. Speed is required in order to perform the calculations without prohibitive dead time. Based on an expected pre-trigger (0, 1 or two charged particles plus energy in the LGD) rate of 10–12 kHz, we need to perform the calculation in about 15 μs. The ADCs must digitize and present their output to the trigger processor in less than 10 μs. Commercially available ADCs are not up to the task either in speed or number of bits. It was decided to design and build a FASTBUS-based ADC system.

Although the ADCs will eventually be packaged as FASTBUS modules with 32 channels per module, for the P2 tests these ADCs were packaged in CAMAC modules, 16 channels per module. The heart of the ADC is the front end which integrates the signal above a pre-sampled baseline and presents the result to two discriminators and a successive-approximation 12-bit digitizer. The two discriminators have separate thresholds and the outputs are available 100 ns after the end of integration for use in a first-level trigger (e.g. multiplicity counting). The background subtraction feature provides good noise immunity and makes possible the realization of the full dynamic range of the ADC. For example, a 60 Hz 1 V amplitude noise added to the signal produces a shift in the output of less than one least count The time required for digitization is 4 μs. Tests have shown that the integral non-linearity is less than one least count. The reset time of 100 ns is an important feature for higher pre-trigger rates.

The characteristics of the custom ADCs are summarized in table 3. In order to construct these modules a factory has been set up in the HEP lab on the Bloomington campus of Indiana University. Surface mount technology is used. The factory [18] includes a station for applying solder paste to a board, a vacuum pickup tool for picking and placing small components and an infrared reflow oven for melting the solder. A computer design program [19] is used for multi-layer board layout. The output is sent to a company [20] which produces the boards. Twenty CAMAC modules were constructed for the P2 tests.

Table 3
Characteristics of the custom-built ADCs

Number of bits	12
Digitizing time	4 μs
Number of channels/CAMAC module	16
Number of channels/FASTBUS module	32
Event readout time for full LGD (FASTBUS) assuming 4 crates reading in parallel and 4% occupancy	5 μs
Reset time (to 1 bit accuracy)	100 ns
Integral non-linearity	0.025%
Other features:	
Noise rejection	
On-board discriminators	

4.3.2. Photon multiplicity trigger

A photon multiplicity trigger was implemented utilizing the discriminated outputs of the custom ADCs. CAMAC multiplicity modules were constructed which used 319 signals [21] corresponding to the input being above threshold 1 and another 319 signals corresponding to the input being above threshold 2. The multiplicity trigger required that N modules have amplitudes above threshold 1 and below threshold 2. The requirement that the modules have a maximum energy was imposed to eliminate charge-exchange events. The common low and high thresholds and the value of N were set under computer control. The procedure for setting these parameters is described below. The state of the discriminators as well as the final answer from the multiplicity units were computer readable. This provided a diagnostic check.

4.4. Monitoring

The monitoring system for P2 is based on a nitrogen laser [22] exciting a small cylinder (0.5-in. thick, 1-in. diameter) of scintillator. The output from the scintillator is fed into a bundle of plastic fibers. One of these fibers goes directly to a phototube which is used to monitor the output of the laser. The other four fibers fan out into an array of Plexiglas bars and nipples, which in turn feed the light into the detector as shown in fig. 20. The four fibers launch light into two ends of two Plexiglas bars, each with 18 Plexiglas nipples placed 4 cm apart. These bars launch light into 18 other bars of similar construction. This system is much less expensive than systems which send a fiber to every module and is much easier to set up and maintain [23].

Several prototype light guides were built and tested. The light guides were 76 cm long, 1 cm thick and 3 cm wide. Each had 18 0.5 in. diameter, 1 cm high nipples glued to it at 4 cm intervals, so that each lead glass module would be fed by its own nipple. Several versions of this bar were tested by launching light into them through a fiber at each end, and measuring the output of each nipple with a phototube. The output from the nipples can be described by:

$$a(e^{-x/k} + e^{-(18-x)/k}), \tag{9}$$

where k is an attenuation length, given in units of blocks (1 block = 4 cm), x is the distance along the bar, also given in blocks. b is a coefficient to account for the difference in fiber output at each end, and a is an amplitude. Various bars were tested: with polished edges, without polished edges, with white paper wrapping, and with aluminized Mylar wrapping. It was

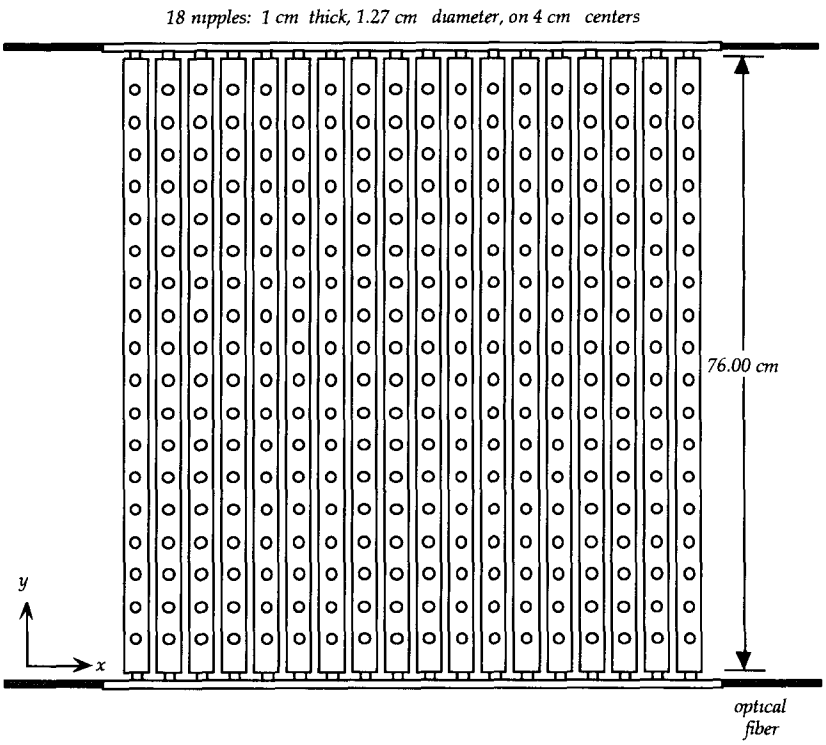

Fig. 20. The array of Plexiglas bars and nipples used to distribute light from four optical fibers, from a nitrogen laser, to 324 lead glass blocks.

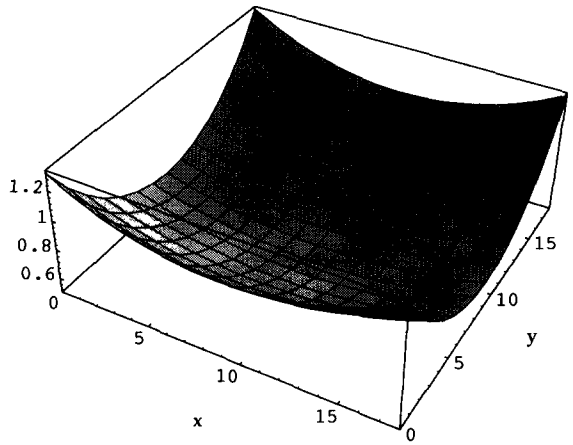

Fig. 21. The variation in light output of the light distribution system shown in fig. 20 (which also shows how x and y are defined). Eq. (9) was used with $k = 12$ blocks for the x variation and $k = 7$ for the y variation.

found that simply polishing the bars gave a $k = 12$ blocks. The wrapping schemes did not significantly improve this value.

A test was then done with a bar being fed by the output of a second bar, instead of with a fiber. The attenuation length in the second bar was found to be 7 blocks. The reason for this discrepancy is that the light from a fiber is launched into the bar in a more collimated forward direction than that from a nipple. This results in a longer attenuation length for the case when light is launched from a fiber since more of the light experiences total internal reflection. Assuming that the launching of light into the four corners of the array is symmetric, the expected light output over the array is shown in fig. 21. The output at the center is about 2.5 times lower than at the corners. There is sufficient light output so that the outputs of all nipples can be equalized by a masking technique. This was not done for the P2 tests.

4.5. Assembling the detector and initial checkout

In anticipation of assembling the full scale LGD, a number of techniques were employed in the P2 assembly. Bar code labels were attached to the cellular wall near each hole. The glass blocks, phototubes and bases were also labeled with a bar code. The bar codes of these elements were read out, in situ, as each block was inserted in the stack and as the phototube/base assemblies were inserted in the wall. The archived information from quality control measurements was also available.

After the system was assembled and connected to the ADCs, the computer controlled high voltage system and the monitoring system were used to check for consistency by turning off all but one module and verifying that the signal reached the correct ADC. After this checkout, the gain versus high voltage characteristics of each module (glass block – phototube – base – ADC) was determined. Finally the monitoring system was used to initially set the high voltage for approximately equal response prior to calibration.

5. Experimental procedure for the P2 tests and results

5.1. The experiment layout

The layout of the experiment is shown in fig. 22. The apparatus was placed in the A3 test beam at BNL. During data-taking, with 15 GeV negative pions, a 1.2 cm thick Be target, corresponding to 3% interaction length, was used. The target was enclosed on four sides by scintillation material and a scintillation counter downstream. Upstream of the target were two scintillation counters to define beam.

The target-to-P2 distance was initially set at 4 m at the incident beam momentum of 15 GeV to scale from the final E852 conditions where the beam energy will be 18 GeV and the target-to-LGD distance will be 5 m.

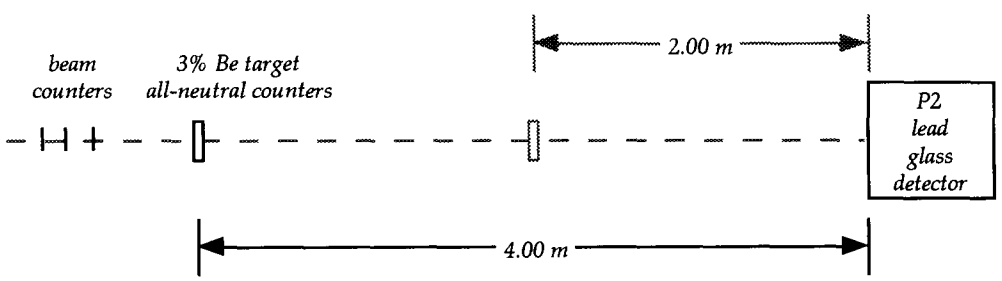

Fig. 22. The experimental layout in the BNL A3 test beam for the P2 tests. For the initial data-taking, the target-to-P2 distance was 4 m. During most of the data-taking, the target-to-P2 distance was 2 m. During calibration the target assembly was removed and a 4 m-long Ar threshold Cherenkov counter was installed for electron tagging.

In both cases, the photons from the most energetic π^0's have a minimum separation of 7.5 cm. For the major part of the data-taking, however, target-to-P2 distance was set at 2 m to maximize the acceptance for higher mass mesons with multi-photon decays.

5.2. Triggers

5.2.1. Data-taking

The all-neutral pretrigger required a beam signal with no signal from the counters on either side and forward of the target. The pre-trigger-rate was approximately 1.5% of the interaction rate. During the data-taking the beam intensity varied from 100 000 π's/pulse to 500 000 π's/pulse, and during most of the run the intensity was below 200 000 π's/pulse, for which the pre-trigger rate was sufficiently low that no other trigger requirements were necessary. The data acquisition system was capable of reading out up to 90 events/spill with less than 10% dead time.

When the beam intensity was above 200 000 π's/pulse, the photon multiplicity trigger described in section 4.3.2 was used. The parameters of this trigger were adjusted to result in a data-taking rate of no more than 90 events/spill. The parameters of the trigger were also determined by using software emulating the multiplicity trigger on a sample of data collected using only the pre-trigger requirement but with the input into the multiplicity trigger read out on an event-by-event basis. The parameters of the trigger were determined by finding the range of values of N and the high and low thresholds, which when applied to data recorded without the multiplicity trigger, maximized the yield of $\eta\pi^0 \to 4\gamma$. At-the same time, the yield of other meson states with multi-photon decays was recorded and compared later to the yields observed with the photon multiplicity requirement in the trigger. To within the accuracy determined by statistics, the observed yields agreed in all cases with the predicted yields.

5.2.2. Other triggers

In addition to the physics triggers described above, pedestal and laser-monitoring triggers were collected throughout the run. Before each accelerator spill, the ADCs were gated and the pedestals recorded. After each accelerator spill the laser was fired and the ADCs recorded. The results of these triggers are discussed in section 5.5.

Data were also recorded using 3 GeV electrons incident on P2 for the purpose of measuring photon position resolution. These results are presented in section 5.6

5.3. Calibration procedure

Prior to data-taking, the calorimeter was calibrated using 3.0 and 5.0 GeV negative beams. The target was removed and a 4 m long atmospheric air threshold Cherenkov counter was installed for tagging electrons. The electron content was approximately 20% of the beam at 3 GeV and 5% of the beam at 5 GeV. The electron flux was approximately 100/pulse at 3.0 GeV.

Before the calibration with beam, the gain vs high voltage function of each module was determined using the laser-based monitoring system (see Section 4.5). The high voltages were also set to yield approximately equal gain from module-to-module, again using the monitoring system. After the 5.0 GeV electron beam was prepared the control of the calibration was transferred to Bloomington, IN using DECNET [24].

The first step was to position the P2 detector, using the computer-controlled transporter, so that the beam was incident on a block near one corner of the detector. The detector was moved horizontally and vertically in 0.5 cm steps to maximize the energy deposition in the block. This determined the beam location relative to the P2 transporter. As a check, the transporter moved the detector so the beam was incident on a block near the opposite corner and the procedure was repeated. The results were consistent. The transporter then moved the detector so that the electron beam was incident on the center of the first block and then proceeded from block to block. At each position about 2 to 3 spills were needed to accumulate adequate statistics. About 15 s was required to calibrate a block at the available intensity or about 80 min for the entire array. A Gaussian fit to the energy distribution in each block was made to determine the mean pulse height in the block. The mean pulse height per block, as a function of block number is shown in fig. 23a after the first 5 GeV scan, before any adjustments were made to the high voltage settings determined by the monitoring system alone. After the first scan of the detector, the software determined a new set of high voltages which were downloaded from Bloomington to the VAX stationII/GPX interfaced to the detector. A second scan at 5 GeV was performed and the results are shown in fig. 23b. Finally a third scan was performed with 3 GeV electrons to check for linearity. The results are shown in fig. 23c.

5.4. Physics triggers

The calibration constants were determined using the data from the 3 and 5 GeV calibration scans using the technique described in section 3.6.1. A cluster-finding algorithm was used to identify photons.

The cluster finding algorithm first constructed a list of module energies and addresses in decreasing order in energy. The module with the largest energy was identified as a cluster center if the module energy exceeded 100 MeV. The module energy was summed with the energies in the eight nearest neighbors. The

coordinates of the photon shower were computed using a linear-weighted average:

$$\langle x\rangle = \frac{\sum_{i=1}^{9} E_i x_i}{\sum_{i=1}^{9} E_i}, \qquad \langle y\rangle = \frac{\sum_{i=1}^{9} E_i y_i}{\sum_{i=1}^{9} E_i}, \tag{10}$$

where E_i is the energy deposited in the ith block and (x_i, y_i) are the coordinates of the ith block. Other techniques for calculating shower position are discussed in section 5.6. The modules associated with a cluster are removed from the list, and the next candidate cluster center and neighbors is analyzed. The yield of events with various numbers of clusters is summarized in table 4.

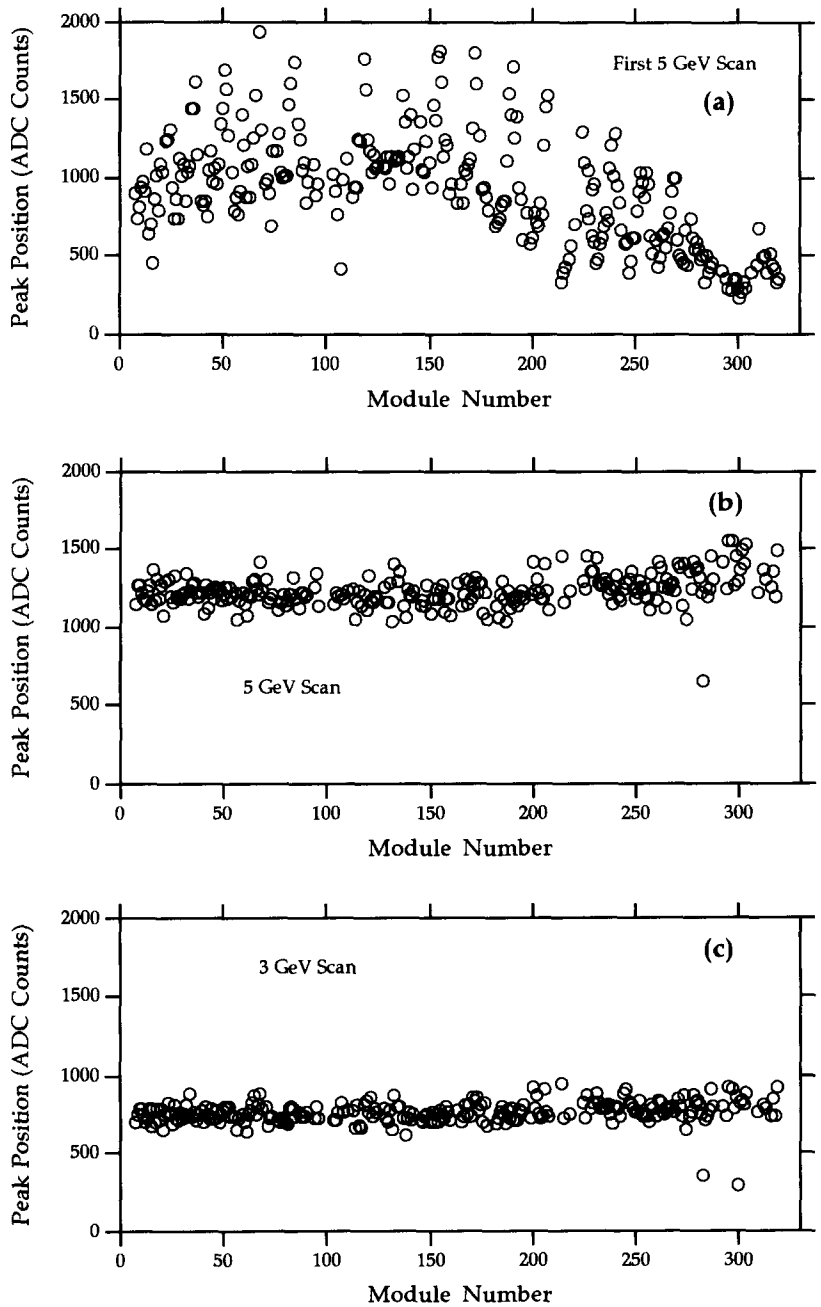

Fig. 23. (a) The position of the electron peak in a module vs module number after the first 5 GeV scan before adjusting the high voltages. (b) The position of the electron peak in a module vs module number after the second 5 GeV scan after adjusting the high voltages as a result of the first scan. (c) The position of the electron peak in a module vs module number after the 3 GeV scan.

Table 4
Fraction [%] of events with found clusters

Number of clusters	4 m neutral trigger	4 m multiplicity trigger	2 m neutral & multiplicity
1	2.8	0.0	8.0
2	24.1	1.7	37.1
3	43.5	44.5	20.8
4	17.0	24.5	16.1
5	8.3	17.8	11.6
6	3.1	7.8	4.2
7	1.3	3.6	1.5
8	0.0	0.0	0.5
9	0.0	0.0	0.1
> 9	0.0	0.0	0.0

5.4.1. 4 m data

With the target-to-P2 distance initially set at 4 m, data were recorded with the all-neutral trigger. The diphoton effective mass distribution for events identified as having two clusters is shown in fig. 24. The π^0 and η decays into two photons are clearly seen. The Gaussian fits to the mass distribution in the vicinity of the π^0 and the η are shown in figs. 25a and 25b respectively. For the π^0, the mass and σ are 134 MeV and 11 MeV while for the η the mass and σ are 542 MeV and 22 MeV. The $\pi^0\pi^0$ effective mass distribution is shown in fig. 26a for those events from the four-cluster sample which are consistent with the hypothesis: $\pi^0\pi^0 \to 4\gamma$. For these events, the photon energies were adjusted in the constrained fit to $\pi^0 \to 2\gamma$. The decay $K^0 \to \pi^0\pi^0$ is clearly observed. The Gaussian fit to the background subtracted distribution

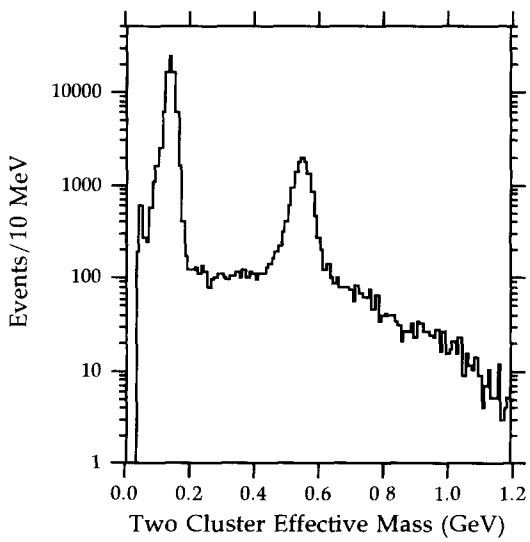

Fig. 24. Two photon effective mass distribution for events with two clusters in the 4 m data sample.

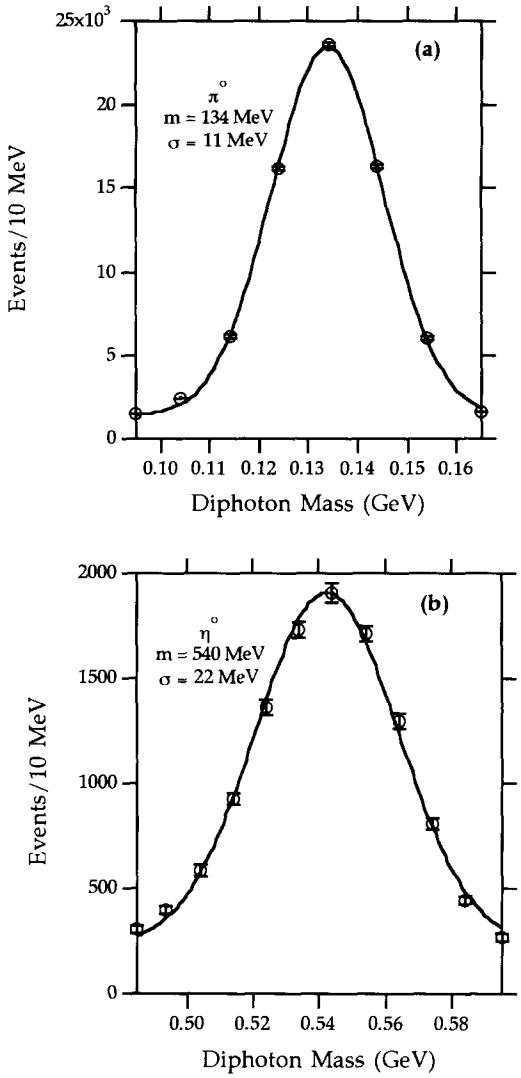

Fig. 25. Fit to the mass distribution of fig. 24 in the (a) π^0 mass region, and (b) in the η mass region.

in the K^0 mass region is shown in fig. 26b. The fit values for the mass and σ are 491 MeV and 21 MeV.

5.4.2. 2 m data

With the target-to-P2 distance set at 2 m, data were recorded with the all-neutral trigger and the multiplicity trigger. The diphoton effective mass distribution for events identified as having two-clusters is shown in fig. 27. The π^0, η and $\eta'(958)$ decays into two photons are clearly seen however with the relative fraction of π^0 to η is suppressed since the minimum diphoton separation for $\pi^0 \to 2\gamma$ at the detector face has been reduced by a factor of two. This also manifests itself in the presence of the ω peak in the spectrum of fig. 27 where the decay $\omega \to \pi^0\gamma \to 3\gamma$ is seen in the two-clus-

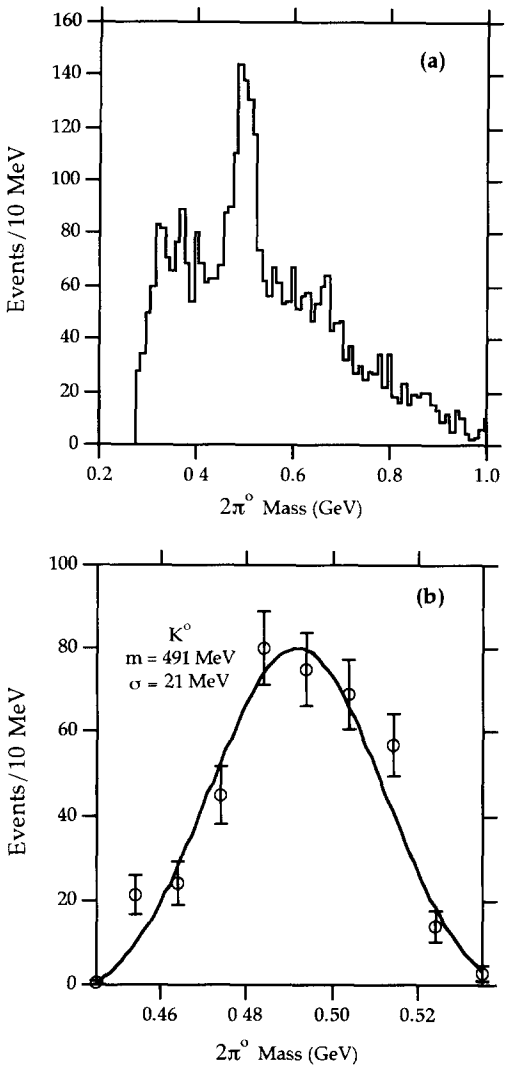

Fig. 26. The $2\pi^0$ effective mass distribution for the 4 m data sample. (b) The $2\pi^0$ effective mass distribution, with background subtraction, in the K^0 mass region, for the 4 m data sample.

ter sample because the photons from the π^0 coalesce at the detector face.

In fig. 28 the $\pi^0\gamma$ effective mass distribution is shown for those events in the three-cluster sample consistent with $\pi^0\gamma \to 3\gamma$. Again a constrained fit was performed on the $\pi^0 \to 2\gamma$ decay. The $\omega \to \pi^0\gamma \to 3\gamma$ decay is observed as well as a peak in the 1250 MeV mass region. The latter peak results from $f_2^0(1270) \to \pi^0\pi^0$, where again one of the $\pi^0 \to 2\gamma$ decays is interpreted as a single photon. The $\pi^0\pi^0$ and $\eta\pi^0$ effective mass distributions are shown in figs. 29 and 30 respectively, for those events from the four-cluster sample which are consistent with the hypothesis: $\pi^0\pi^0 \to 4\gamma$ and $\eta\pi^0 \to 4\gamma$. Again, constrained fits to the decays

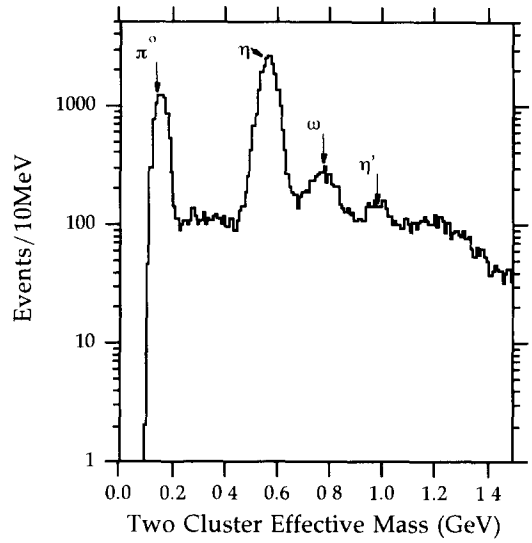

Fig. 27. The diphoton mass spectrum for two cluster events in the 2 m data sample.

$\pi^0 \to 2\gamma$ and $\eta \to 2\gamma$ were performed. In fig. 29 there is a hint of the decay $K^0 \to \pi^0\pi^0$ and the decay $f_2^0(1270) \to \pi^0\pi^0$ is observed. In fig. 30, the decays $a_0(980) \to \eta\pi^0$ and $a_2(1320) \to \eta\pi^0$ are seen.

5.5. Pedestal and laser-monitor data

During the data-taking, pedestal and laser-monitor triggers were recorded prior to and after each accelerator spill, respectively. In fig. 31, the plot of ADC pedestal value vs module number is shown for a period

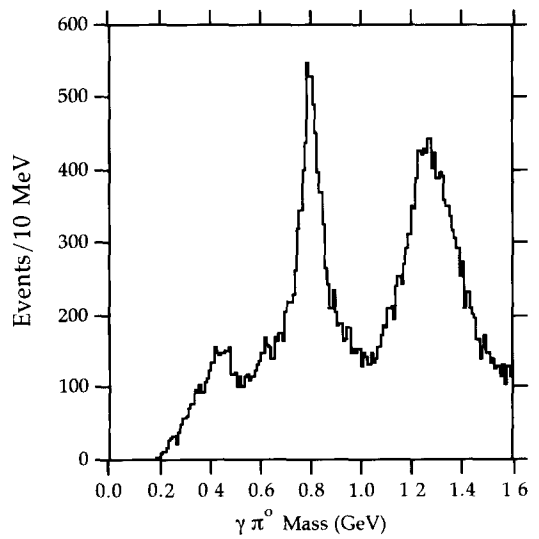

Fig. 28. The $\pi^0\gamma$ effective mass spectrum for three-cluster events in the 2 m data sample

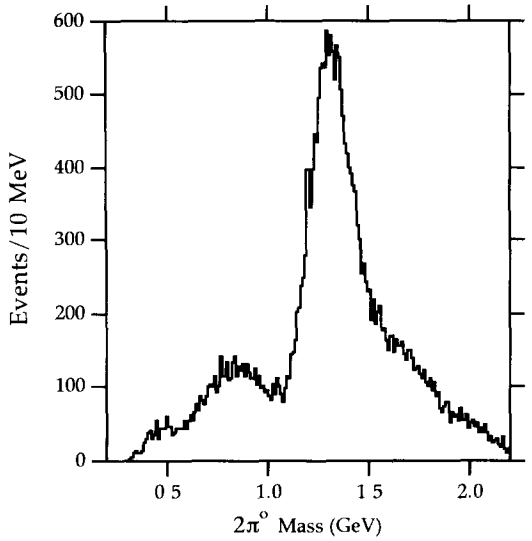

Fig. 29. The $2\pi^0$ effective mass spectrum for four-cluster events in the 2 m data sample.

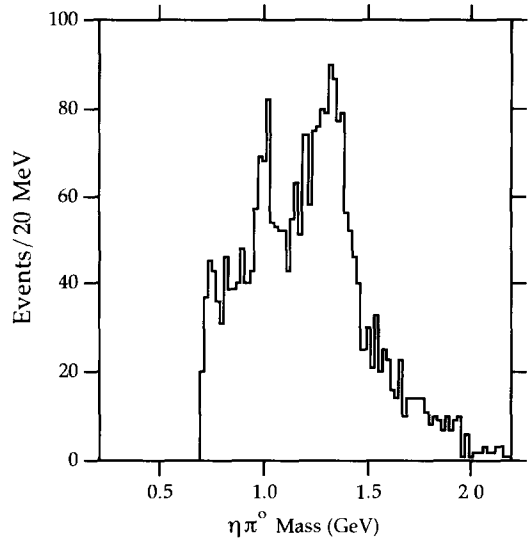

Fig. 30. The $\eta\pi^0$ effective mass spectrum for four-cluster events in the 2 m data sample.

of running covering approximately two weeks. The error bars are the standard deviation in the pedestal distribution over the period. In fig. 32, the variation of pedestal for three representative modules is shown as a function of run number over the two week period. These distributions indicate that the pedestal variation from module to module and the module variation over time are small.

In fig. 33 the normalized laser response, averaged over all modules, is shown as a function of run number. The response is normalized by taking the ratio of a module response to the response from a phototube looking directly at a fiber (no lead glass involved) illuminated by the laser. Thus, pulse-to-pulse variations in laser output are removed.

5.6. Position resolution

5.6.1. Algorithms

Three algorithms were considered to determine the calculated impact coordinates (x_c, y_c) of a particle initiating an electromagnetic shower on the face of the

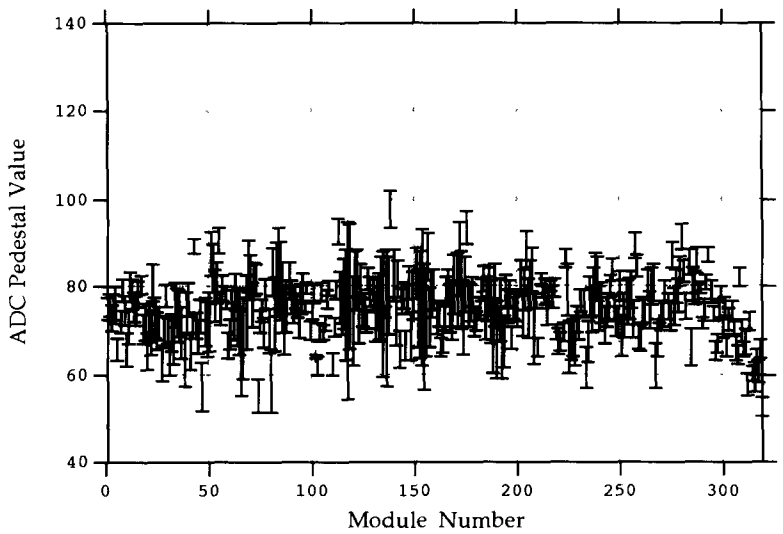

Fig. 31. Variation of ADC pedestal value vs module number. The error bars represent the s of the pedestal distribution over a 2 week period.

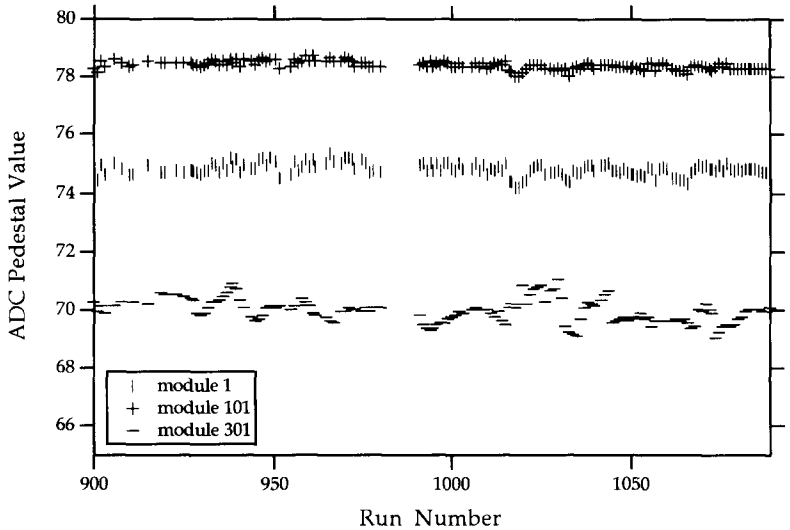

Fig. 32. Variation of ADC pedestal value vs time (a 2-week period) for 3 representative modules.

lead glass array. Each uses a weighted mean:

$$x_c = \frac{\sum_j^N w_j(E_j)\, x_j}{\sum_j^N w_j(E_j)}. \tag{11}$$

The sum is typically carried out over nine (twenty-five) modules defining a cluster, the cluster center (module with energy greater than 50 MeV and with the largest energy in the cluster) and its eight (twenty-four) nearest neighbors. The weight, $w_j(E_j)$, is a function of the energy in the cluster and x_j is the coordinate of the center of the jth module in the cluster. A similar procedure defines y_c.

In the studies described below nine modules (3×3 array) were used to define the cluster. Our studies were repeated using a 5×5 array and in all cases the relative improvement in coordinate resolution was less than 2%.

Motivated by the work of others [25] we considered three weighting functions

$$w_j^{(1)}(E_j) = E_j, \tag{12}$$

$$w_j^{(2)}(E_j) = E_j^{\mathrm{r}}, \tag{13}$$

$$w_j^{(3)}(E_j) = \mathrm{Max}\{0,\ a_0 + \ln(E_j) - \ln(E_{\mathrm{tot}})\}, \tag{14}$$

where a_0 is a constant and E_{tot} is the total energy in the N modules defining the cluster. We refer to $w_j^{(1)}$,

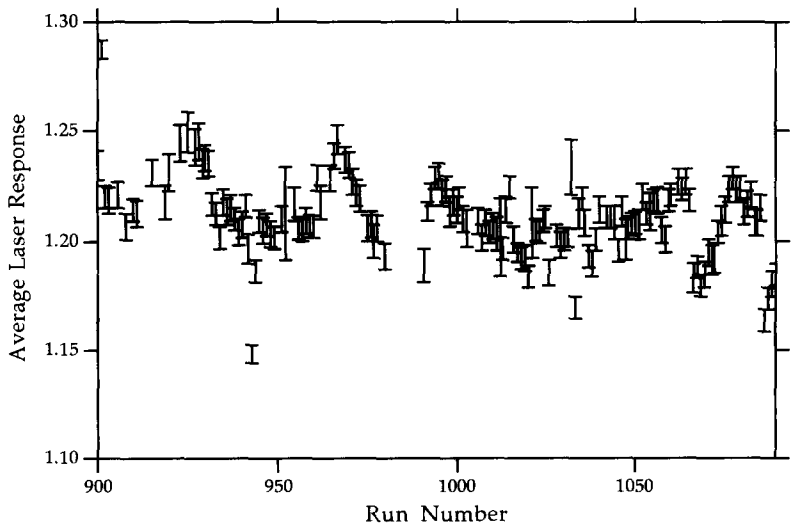

Fig. 33. Variation of average normalized laser response vs run number (covering a 2 week period).

Table 5
Coordinate resolution (σ) in mm for the three algorithms considered in the Monte Carlo (MC) studies and P2 data

Energy [GeV]	Linear	Power	Logarithmic
1 (MC)	8.2	5.4	4.9
3 (MC)	9.9	5.4	3.3
3 (P2)	6.0	5.5	4.1
5 (MC)	10.1	5.4	2.8
10 (MC)	11.3	6.6	2.2
15 (MC)	14.9	8.1	1.8
25 (MC)	37.9	20.5	1.6

$w_j^{(2)}$ and $w_j^{(3)}$ as linear, power and logarithmic weighting.

5.6.2. Monte Carlo studies

The program GEANT [26] was used to simulate the energy deposition in a 5×5 array of lead glass modules induced by incident photons of six different energies (1, 3, 5, 10, 15 and 25 GeV) uniformly illuminating the central module. The simulation included the effect of the measured LGD energy resolution (Eq. 5), ADC threshold and quantization. The coordinate resolution ($\sigma_{x,y}$) was obtained by fitting to a Gaussian function, the distributions in the difference between the calculated and actual coordinates. The results are shown in table 5. In determining the power, r, and the constant, a_0, to use, we studied the variation in σ_x as a function of these parameters. The results are shown in figs. 34 and 35 for r and a_0 respectively as a function of energy. In table 5, the values of r and a_0 which optimize the coordinate resolution are used for each energy. The variation in r is from 0.58 at 1 GeV to 0.63 at 25 GeV while a_0 varies from 4.1 at 1 GeV to 4.3 at 25 GeV. The logarithmic weighting, which is motivated by the exponential fall-off of the transverse energy profile, yields the best results of the three algorithms.

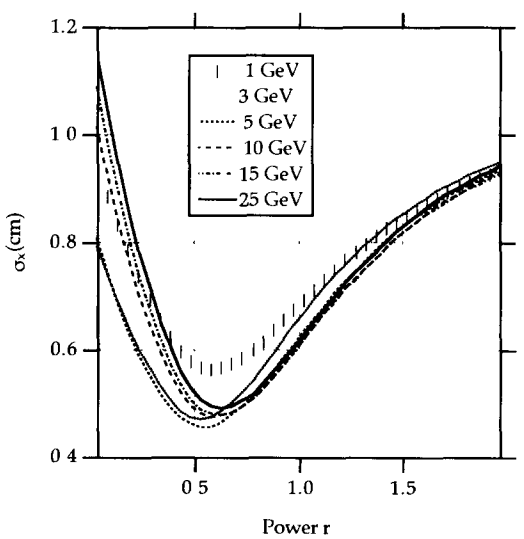

Fig. 34. Variation of the power r in the power algorithm (see eq. (13)) as a function of coordinate resolution for Monte Carlo data at various energies.

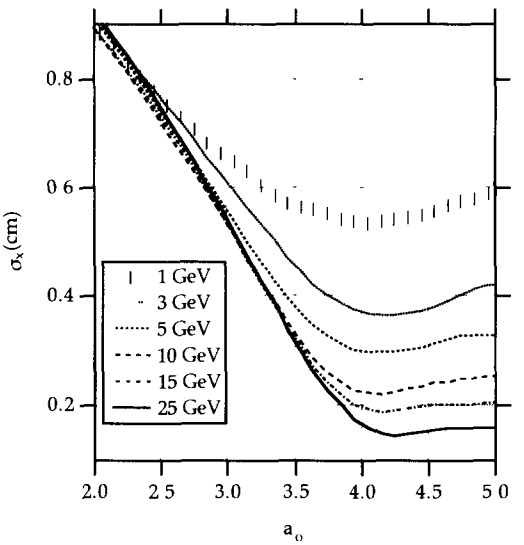

Fig. 35. Variation of a_0 in the logarithmic algorithm (see eq. (14)) as a function of coordinate resolution for Monte Carlo data at various energies.

5.6.3. Position resolution information from the P2 data

During the P2 test run, data were collected to study position resolution. The P2 array was illuminated by a 3 GeV, normally incident, electron beam. Starting with the beam incident at the center of one module, the P2 array was moved horizontally in 5 mm steps to the centers of the neighboring modules. At each of the 17 positions, 4000 triggers were collected. Since the width of the incident beam was large compared to the expected position resolution, two pairs of overlapping scintillation counters were used to define the beam position to within ± 4 mm.

The distribution in the difference between the calculated and actual coordinates, $(x_{\text{calc}} - x_{\text{real}})$, are shown in fig. 36 for the three different algorithms. The values of r and w_0 were varied to minimize the width of the distributions for the data and were found to be 0.73 and 3.45 respectively, to be compared to 0.53 and 4.15 for the Monte Carlo simulations at 3 GeV. A fit of the distributions to a Gaussian function yields the following resolutions σ_x: 6.0 mm for the linear algorithm, 5.5

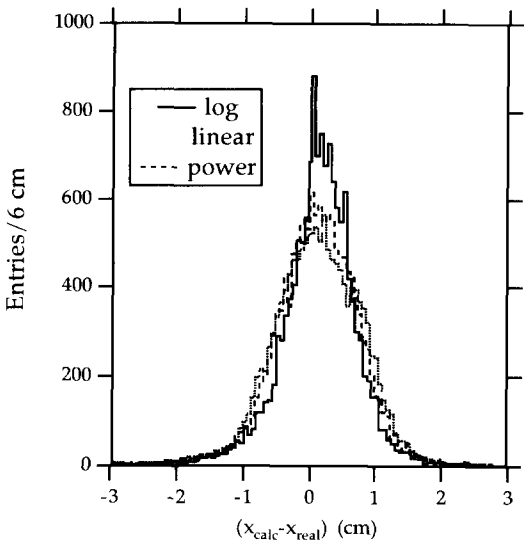

Fig. 36. Distribution in the difference between calculated and actual coordinates for the P2 3 GeV electron data for the three algorithms.

mm for the power algorithm and 4.7 mm for the logarithmic algorithm.

6. Summary

The design, construction and test results of two prototype lead glass calorimeters, a 25-element and a 319-element detector, including the high voltage system and ADC system, were described. These calorimeter prototypes were built in preparation for the construction of a 3053-element lead glass detector to be used as part of BNL AGS experiment 852, a search for mesons with unusual quantum numbers. Quality control procedures employed in the construction of the prototypes and full-scale detector were also described. Results were presented on energy resolution, position resolution, and observation of the decays of mesons into multi-photon final states. Performance of the hardware including the calibration system and laser-monitoring system was described.

Acknowledgements

We thank the staffs of the participating institutions and the assistance of Brookhaven National Lab. In the US, this work was supported in part by DoE grants DE-FG02-91ER40661 at Indiana University and DE-FG02-91ER40623 at the University of Notre Dame, by NSF grants PHY-9213982 at the University of Louisville, PHY-9001389 at the University of Massachusetts Dartmouth and PHY-9120649 at the University of Notre Dame. In Russia, this work was supported in part by the Ministry of Science, Highest School and Technical Policy of Russian Federation and the USSR State Committee for Utilization of Atomic Energy.

References

[1] B.B. Brabson et al., AGS Proposal P852: A Search for Mesons with Unusual Quantum Numbers, submitted to the BNL Program Committee in November, 1989.
[2] The glass was produced in the Industry for Optical Glass in Moscow, Russia.
[3] F. Binon et al., Nucl. Instr. and Meth. A248 (1986) 86.
[4] Shimadzu Model UV-160 spectrophotometer.
[5] Rohlix actuators Rohlix model 1111, Zero-Max, 2845 Harriet Avenue South, Minneapolis, MN 55408-2291, USA.
[6] Heidenhhain pneumatic probes, model MT12P, Heidenhhain Corporation, 115 Commerce Drive, Schaumburg, IL 60173, USA.
[7] Manufactured by TECA Inc.
[8] Sylgard 184 optical gel made by Dow-Corning.
[9] Laser Science Inc. model VSL-337ND nitrogen laser.
[10] Hamamatsu type S1772-02.
[11] Manufactured by General Fiber Optics.
[12] Hewlett-Packard HLMP-1503 LED (569 nm).
[13] J.J. Gomez et al., Nucl. Instr. and Meth. A262 (1987) 284;
R. Engelmann et al., Nucl. Instr. and Meth. 216 (1983) 45.
[14] The transporter used in the P2 tests was kindly loaned to us by Prof. Masaike of Kyoto University.
[15] We used a PK130M Compumotor drive controller running a 13A Rm162-308 stepping motor. This motor can step 2000 steps per revolution. When the motor is at a 1 kHz step rate it is rated to lift 65000 lbs. The controller and driver are manufactured by Parker Hannifin Corp, Rohnert Park, CA. The drive controller was controlled via CAMAC through a Joerger stepping motor controller SMC24BP. This controller was 24 bits and had programmable acceleration and speed.
[16] The SMC24B controller has inputs for upper and lower limits. This was used to form the first level of interlock protection. Just beyond the first interlock switch was the switch for the second level, a SCR-based switching system. If the switch was triggered then the power to the entire drive system was cut. This also engaged the brakes on the vertical drive system. The brakes by Matrix Engineering are rated at 80000 lbs.
[17] The encoders by BEI Motion System Company have a resolution of $\pm 1/512$ of a revolution. They were bolted in position and then the shafts were mechanically coupled on the encoder end with a flexible coupling to a rod which was chemically bonded to the ball screw that was part of the drive system.
[18] The manufacturers of the stations used in the ADC factory: OK Industries Inc, 3455 Conner St., Bronx, NY

10475, EFD, 977 Waterman Ave, East Providence, RI 02914 and Nu-Concept Systems, 2725 Advance Lane, Colmar, PA 18915, USA.
[19] Sci-Cards electronics design package.
[20] Excel Circuits Co., Auburn Hills, MI 48057, USA.
[21] Although the P2 stack was nominally 18×18, the four corner blocks were not instrumented. Furthermore the lead glass block near the center was not present; it was replaced by an aluminum channel so 319 modules were instrumented.
[22] Laser Photonics LN-300C nitrogen laser.
[23] We acknowledge E. Kistenev of IHEP and BNL who suggested this technique of light distribution to us.
[24] The precision and beam time required for calibration of the lead glass detector is of concern. In order to make the most efficient use of beam time and in order to exercise care in the calibration two parallel crews, one at the experiment, and one off-site were involved in the calibration. We plan to use this technique in the calibration of the full-scale LGD.
[25] G.A. Akopjanov et al., Nucl. Instr. and Meth. 140 (1977) 441;
V.A. Davydov et al., Nucl. Instr. and Meth. 145 (1977) 267;
F. Binon et al., Nucl. Instr. and Meth. 188 (1981) 507;
F. Binon et al., Nucl. Instr. and Meth. 206 (1983) 373;
F. Binon et al., Nucl. Instr. and Meth. A248 (1986) 86;
L. Bartoszak et al., Nucl. Instr. and Meth. A301 (1991) 47;
G.S. Bitzadze et al., Nucl. Instr. and Meth. A311 (1992) 472;
T.C. Awes et al., Nucl. Instr. and Meth. A311 (1992) 130.
[26] R. Brun et al., CERN Data Handling Division Report DD/EE/84-1, GEANT 3 Manual (1984).